nature electronics

Article

https://doi.org/10.1038/s41928-026-01590-8

High-mobility holes in gallium nitride and their quantum oscillations

Received: 10 February 2025

Accepted: 16 February 2026

Published online: 23 March 2026

Check for updates

Chuan F. C. Chang[1] ✉, Joseph E. Dill[2], Zexuan Zhang[3], Jie-Cheng Chen[4,5], Naomi Pieczulewski[6], Samuel J. Bader[2,9], Oscar E. Ayala Valenzuela[7], Scott A. Crooker[7], Fedor F. Balakirev[7], Ross D. McDonald[7], Jimy Encomendero[3], David A. Muller[2,8], Feliciano Giustino[4,5], Debdeep Jena[3,6,8] ✉ & Huili Grace Xing[3,6,8] ✉

Gallium nitride (GaN) is used in solid-state lighting and in high-performance radio frequency and power electronics. However, due to inefficient hole doping and low hole mobility, quantum oscillations in p-type GaN have not been observed, which limits studies of valence bands and hole transport engineering. Here we report high hole mobilities in a polarization-induced two-dimensional hole gas at a gallium nitride/aluminium nitride interface. The holes degenerately occupy two valence bands of GaN—the light-hole and heavy-hole bands—and have mobilities of 2,000 $cm^2 V^{-1} s^{-1}$ and 400 $cm^2 V^{-1} s^{-1}$ at 2 K, respectively. We use Shubnikov–de Haas oscillations of holes from both valence bands to extract their respective sheet densities and quantum scattering times and the effective masses of light holes and heavy holes. The hole mobilities of our heterostructure highlight the possibility of developing cryogenic GaN complementary metal–oxide–semiconductor technology with potential applications in quantum computing control electronics.

The discovery of p-type doping in the wide-bandgap semiconductor gallium nitride (GaN) led to the development of blue light-emitting diodes and lasers[1]. GaN high-electron mobility transistors are also used in energy-efficient radio frequency and power electronics because of their fast switching, enabled by high electron mobility[2–4]. Consequently, there is interest in using p-channel GaN transistors for integrated complementary circuits[5–11]. Shubnikov–de Haas (SdH) quantum oscillations of electrons in GaN were observed in 1992, immediately after the discovery of two-dimensional electron gases (2DEGs) at AlGaN/GaN heterojunctions and before the origin of these 2DEGs was understood to be due to polarization discontinuity[12]. However, the analogue of the polarization-induced 2DEG, the two-dimensional hole gas (2DHG) in GaN without impurity doping, was only discovered in 2019[13]. As GaN holes have lower mobility and are harder to access experimentally, fundamental understanding of the 2DHG has lagged behind that of the 2DEG.

SdH oscillations—the oscillation in electrical resistance under a magnetic field due to the formation of Landau levels (LLs)—are a powerful and widely used tool to probe the band structures and Fermi surfaces of new materials and phases of matter[14–17]. SdH oscillations observed in the technologically dominant semiconductors—silicon, germanium, GaAs and n-type GaN—have helped shape understanding of their physics by allowing measurements of their Fermi surface geometry, effective masses, band non-parabolicity, quantum scattering times, gyromagnetic ratio and spin–orbit coupling[12,18–26]. The high mobility of charge carriers in these materials, a testament to continual

[1]Department of Physics, Cornell University, Ithaca, NY, USA. [2]School of Applied and Engineering Physics, Cornell University, Ithaca, NY, USA. [3]School of Electrical and Computer Engineering, Cornell University, Ithaca, NY, USA. [4]Department of Physics, The University of Texas Austin, Austin, TX, USA. [5]Oden Institute for Computational Engineering and Sciences, The University of Texas Austin, Austin, TX, USA. [6]Department of Materials Science and Engineering, Cornell University, Ithaca, NY, USA. [7]National High Magnetic Field Laboratory, Los Alamos National Laboratory, Los Alamos, NM, USA. [8]Kavli Institute at Cornell for Nanoscale Science, Ithaca, NY, USA. [9]Present address: Foundry Technology Research, Intel Corporation, Hillsboro, OR, USA.
✉e-mail: cc2737@cornell.edu; djena@cornell.edu; grace.xing@cornell.edu

improvements in crystal growth and processing, have enabled the observation of integer and fractional quantum Hall effects, revealing a range of geometric and topological effects on the Hall conductance[27–30]. SdH oscillations of holes have been observed in diamond[31,32] but not yet in other wide-bandgap semiconductors.

Observing SdH oscillations requires mobile carriers and electrical contacts that survive cryogenic temperatures, alongside high carrier mobility. The thermal freeze-out of holes in magnesium (Mg)-doped GaN[8,33] conflicts with the cryogenic nature of SdH experiments, where the thermal energy must be small compared to cyclotron energy: that is, $k_B T < \hbar\omega_c$ (k_B is the Boltzmann constant, T is the absolute temperature, $\hbar$ is the reduced Planck's constant, and $\omega_c = eB/m$ is the cyclotron frequency, where e is elementary charge, B is the magnetic field, and m is the cyclotron effective mass). Furthermore, the formation of ohmic contact with p-type GaN is challenging even at room temperature due to the lack of metals with sufficiently large work functions to contact GaN's deep valence band lying 7.5 eV below the vacuum level[10,34]. Finally, hole mobility must be sufficiently high to satisfy the condition $\mu_q B > 1$, where μ_q is the quantum mobility. At $B = 25$ T, the quantum mobility, which is typically smaller than the Hall or field-effect mobility, must itself be larger than 400 $cm^2 V^{-1} s^{-1}$ to observe SdH oscillations.

In this Article, we report high mobilities in a polarization-induced 2DHG in GaN and their SdH oscillations. Using band-resolved Hall effect measurements, we observe parallel conduction of two groups of holes showing mobilities of around 2,000 $cm^2 V^{-1} s^{-1}$ and 400 $cm^2 V^{-1} s^{-1}$ at 2 K. Longitudinal magnetoresistance measurements reveal two distinct sets of SdH oscillations. The effective masses extracted from these oscillations identify the two types of holes as originating from the light-hole (LH) and heavy-hole (HH) bands. These results provide direct metrology of GaN's valence bands and offer insights into hole transport. The demonstration of high hole mobilities at cryogenic temperatures suggests a route to cryogenic GaN complementary metal–oxide–semiconductor (CMOS) technology operating near 5 V, which could lead to the development of compact and simple control electronics for quantum technology applications.

Polarization-induced 2DHG in a gallium nitride/aluminium nitride heterostructure

Figure 1a shows a schematic of the heterostructure grown by molecular beam epitaxy (MBE). A thin layer of GaN is grown to ensure pseudomorphic compressive strain to AlN, giving an atomically sharp interface as shown in the annular dark field (ADF) scanning transmission electron microscopy (STEM) image of a representative sample (Fig. 1b). Details on sample preparation can be found in Methods.

Mobile holes are induced electrostatically by a fixed negative sheet charge arising from the polarization discontinuity between GaN and AlN. This doping scheme, known as polarization doping, does not require Mg dopants and prevents carrier freeze-out at cryogenic temperatures. As shown in the band diagram (Fig. 1c), a triangular quantum well (QW) at the gallium nitride/aluminium nitride (GaN/AlN) interface confines these holes. A self-consistent Schrödinger–Poisson calculation (Methods) suggests the Fermi level E_F in the QW lies ~60 meV below the GaN valence band maximum (VBM), creating a degenerate 2DHG in both the first HH and the first LH subbands of the QW (Fig. 1c, inset). Although not required to induce the 2DHG[13,35], an epitaxial layer of Mg-doped GaN is added to establish good electrical contact to the buried 2DHG down to 2 K (Fig. 1d).

Figure 1e shows that sheet resistance R_{sh} of the 2DHG, measured at $B = 0$ T, decreases with temperature, confirming the metallic nature of the 2DHG. At 10 K, R_{sh} reaches 220 Ω sq^{-1}—five times lower than in our earlier work[13]. Figure 1e also shows the apparent Hall mobility (Extended Data Fig. 1) of both samples, confirming that the improvement in R_{sh} in this work stems primarily from increased hole mobility. In fact, the present 2DHG constitutes the lowest-resistance p-type channel reported in III-nitrides across all temperatures.

The high crystal quality in the present sample results from several key innovations in III-nitride growth by plasma-assisted MBE. These include the use of impurity-blocking layers to prevent compensation by n-type impurities[36], the use of bulk AlN single crystals as the substrate[37] and the application of in situ cleaning[38,39] and heterostructure growth techniques[35] developed for bulk AlN substrates (Methods).

At 300 K, Hall effect measurement (Fig. 1g, inset) shows that the Hall resistance $R_{Hall} = V_{Hall}/I_x$ (used interchangeably with R_{xy}) is linear in B up to ±9 T (Fig. 1f, inset). The positive slope confirms p-type transport. A table-top Hall measurement that uses a small magnetic field (typically <1 T) can be used to extract an apparent Hall density $n_{apparent} = 1/eR_H$, where R_H is the slope of R_{Hall} in the small-field range, and an apparent Hall mobility is extracted as $\mu_{apparent} = R_{sh}/R_H$ (Extended Data Fig. 1). At low temperatures, however, R_{Hall} becomes nonlinear with B (Fig. 1f, inset), suggesting parallel conduction of two types of holes with distinct mobilities. As detailed in Supplementary Note I, when R_{Hall} and the longitudinal resistance R_{xx} have contributions from two hole channels, the apparent mobility obtained at small field ($B \to 0$ T) is equal to the conductivity-weighted average of each channel's mobility: that is,

$$\mu_{\text{apparent}} = \langle\mu\rangle = \left(\sum \sigma_i \mu_i\right) / \left(\sum \sigma_i\right),$$

where $\sigma_i = en_i\mu_i$ is each hole band's conductivity and μ_i and n_i are each band's mobility and density, respectively.

To extract μ_i and n_i individually, we fit $R_{xx}(B)$ and $R_{xy}(B)$, measured up to ±9 T at each temperature, to the two-channel Drude model as demonstrated in Extended Data Fig. 1. The extracted mobilities are shown in Fig. 1f and in Extended Data Fig. 1c as a function of temperature, and the extracted densities are shown in Extended Data Fig. 1d. We tentatively assign the higher-density, lower-mobility holes to the HH band ($n_{HH}^{Hall} \approx 5 \times 10^{13}$ cm^{-2} and $\mu_{HH} \approx 400$ $cm^2 V^{-1} s^{-1}$ at 2 K) and the lower-density, higher-mobility holes to the LH band ($n_{LH}^{Hall} \approx 5 \times 10^{12}$ cm^{-2} and $\mu_{LH} \approx 2{,}000$ $cm^2 V^{-1} s^{-1}$ at 2 K). The two-channel fitting is performed up to 100 K, above which there are insufficient polynomial features in $R_{xx}(B)$ and $R_{xy}(B)$ in the ±9 T window to constrain the fit[40], although parallel conduction of HHs and LHs is nevertheless expected to persist (Supplementary Note I).

As shown in Fig. 1f, the temperature dependence of μ_{LH} and μ_{HH} is well-described by Matthiessen's rule: $1/\mu_{LH/HH} = 1/\mu_{LH/HH}^{extr} + 1/\mu_{LH/HH}^{intr}$, where $\mu_{LH/HH}^{extr}$ is a temperature-independent mobility limit due to extrinsic scattering (that is, due to interface roughness, dislocations, impurities, and so on) and $\mu_{LH/HH}^{intr}$ is the mobility limit due to intrinsic scattering (for example, due to phonons), with a power-law temperature dependence. At low temperature, phonon scattering is suppressed and extrinsic scattering dominates; mobilities at low temperature thus serve as an indicator of crystal quality. Extrapolating to 300 K, where phonon scattering dominates, we estimate μ_{HH} to be 18 $cm^2 V^{-1} s^{-1}$ and μ_{LH} to be 72 $cm^2 V^{-1} s^{-1}$, together giving an apparent mobility of $\langle\mu\rangle = 32$ $cm^2 V^{-1} s^{-1}$ at 300 K.

Before proceeding to the quantum oscillation results, we make another remark on the comparison between the present sample and that in our earlier work[13], which reported only $\langle\mu\rangle$. As shown in Fig. 1e, despite substantial (>400%) improvement in the low-temperature $\langle\mu\rangle$ due to improved crystal growth, the improvement at 300 K is much smaller: from $\langle\mu\rangle = 25$ $cm^2 V^{-1} s^{-1}$ to 32 $cm^2 V^{-1} s^{-1}$. This discrepancy further confirms that the 300 K mobility of the present sample is near the intrinsic, phonon-limited value. Thus, to achieve higher room-temperature hole mobility (>50 $cm^2 V^{-1} s^{-1}$) for n–p-balanced GaN CMOS, it is necessary to move beyond crystal growth and employ strategies such as strain engineering of hole effective masses to boost mobility at all temperatures[6,7]. Nevertheless, these high hole mobilities at cryogenic temperatures suggest the crystal quality achieved to date is sufficient to demonstrate high-speed cryogenic GaN CMOS.

https://doi.org/10.1038/s41928-026-01590-8

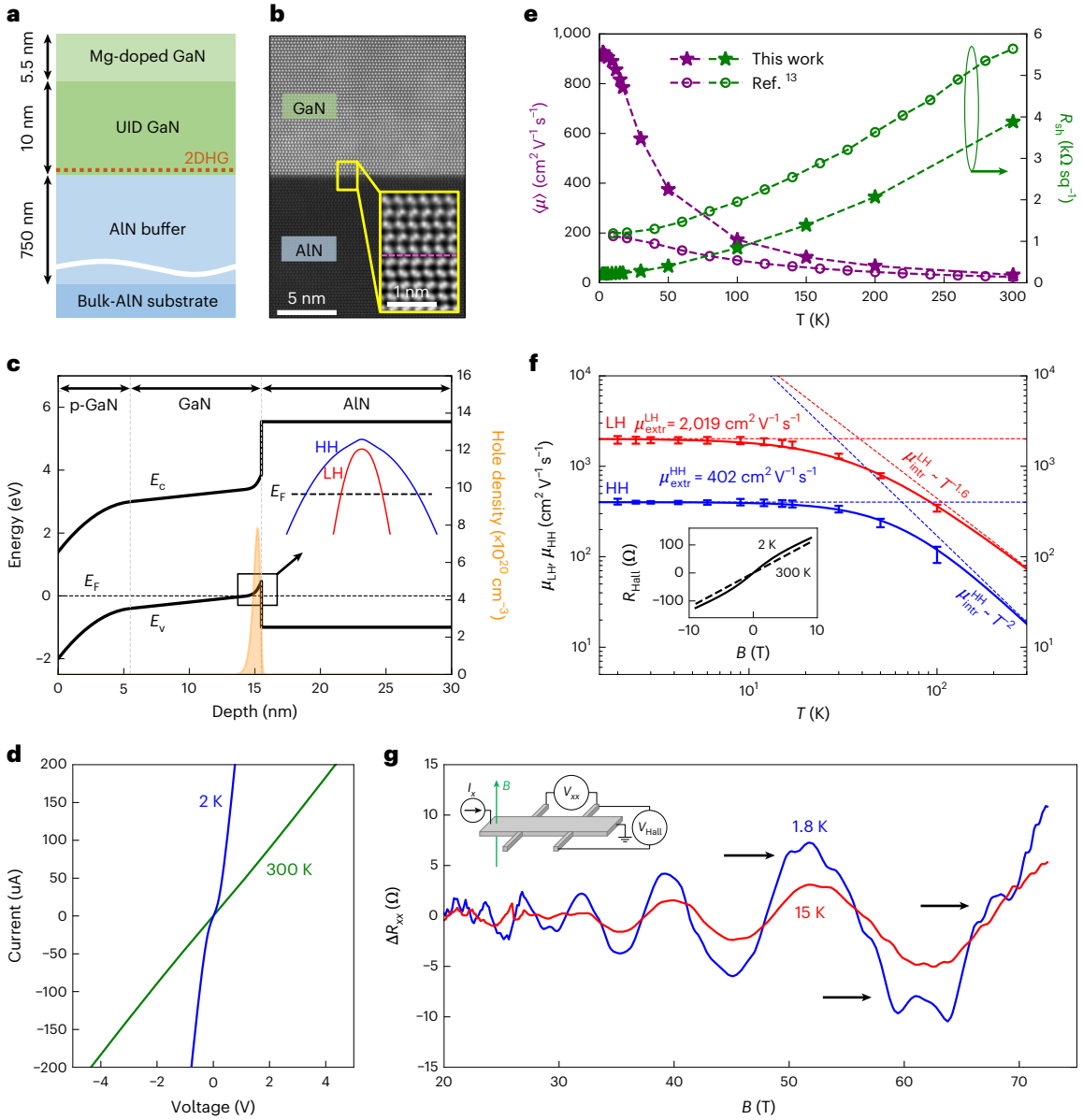

Fig. 1 | Structural and transport properties of a GaN/AlN 2DHG. a, Schematic of the GaN/AlN heterostructure grown by MBE. A 2DHG forms in the unintentionally doped (UID) GaN layer near the GaN/AlN interface. **b**, ADF scanning transmission electron microscopy image of a representative sample showing an atomically sharp GaN/AlN interface. Inset, integrated differential phase contrast image showing the metal polarity of the heterostructure. **c**, Energy band diagram of the heterostructure showing the conduction band edge (E_c), valence band edge (E_v) and Fermi level (E_F) versus depth from the surface. A QW forms at the GaN/AlN interface, confining a 2DHG that degenerately occupies both the first HH and LH subbands. **d**, Two-point I–V curve of the sample, showing ohmic behaviour at 300 K and slightly Schottky behaviour at 2 K. **e**, Apparent mobility $\langle\mu\rangle$ (main text and Extended Data Fig. 1) and sheet resistance R_{sh} of the 2DHG versus temperature, compared with our previous report. **f**, LH and HH mobilities versus temperature. Extraction methods and error bar definitions are provided in Extended Data Fig. 1 and Supplementary Note I. Dashed lines represent extrinsic ($\mu^{extr}_{LH/HH}$) and intrinsic ($\mu^{intr}_{LH/HH}$) mobility limits, and solid lines show the total mobility calculated via Matthiessen's rule $\mu^{-1}_{tot} = \mu^{-1}_{extr} + \mu^{-1}_{intr}$. Inset: R_{Hall} measured up to 9 T at 2 K and 300 K confirms p-type conduction. Nonlinearity at low temperatures suggests parallel conduction of LHs and HHs. **g**, Quantum oscillations in R_{xx} versus B, after background subtraction (Methods and Extended Data Fig. 4). Arrows indicate an additional oscillation component emerging at low temperatures and high fields. Inset, schematic of the Hall bar used for transport measurements. Panel **e** adapted with permission from ref. 13, AAAS.

SdH oscillations of HHs and LHs

SdH oscillations in R_{xx} are measured in a Hall bar as a function of perpendicular magnetic field applied up to 72 T. The Fig. 1g inset shows a schematic, and Extended Data Fig. 2 shows optical images of the fabricated Hall bar. After subtracting a smooth polynomial background, the oscillations ΔR_{xx} are plotted with respect to B in Fig. 1g, and no additional data smoothing is performed. Extended Data Fig. 3 shows R_{xx} profiles measured at various temperatures and under different current injection levels. Extended Data Fig. 4 shows R_{xx}, its polynomial background and the corresponding ΔR_{xx} at various temperatures. The detailed procedure to determine the background and its impact on effective mass and quantum mobility extractions are provided in Supplementary Fig. 1 and Supplementary Table 1.

Characteristic of quantum oscillations, the amplitude grows with increasing magnetic field and with decreasing temperature. Cooling from 15 K to 1.8 K, we observe another set of oscillations resolvable above 50 T. In the following, we show that these small-amplitude, high-frequency oscillations are due to the low-mobility but high-density

https://doi.org/10.1038/s41928-026-01590-8

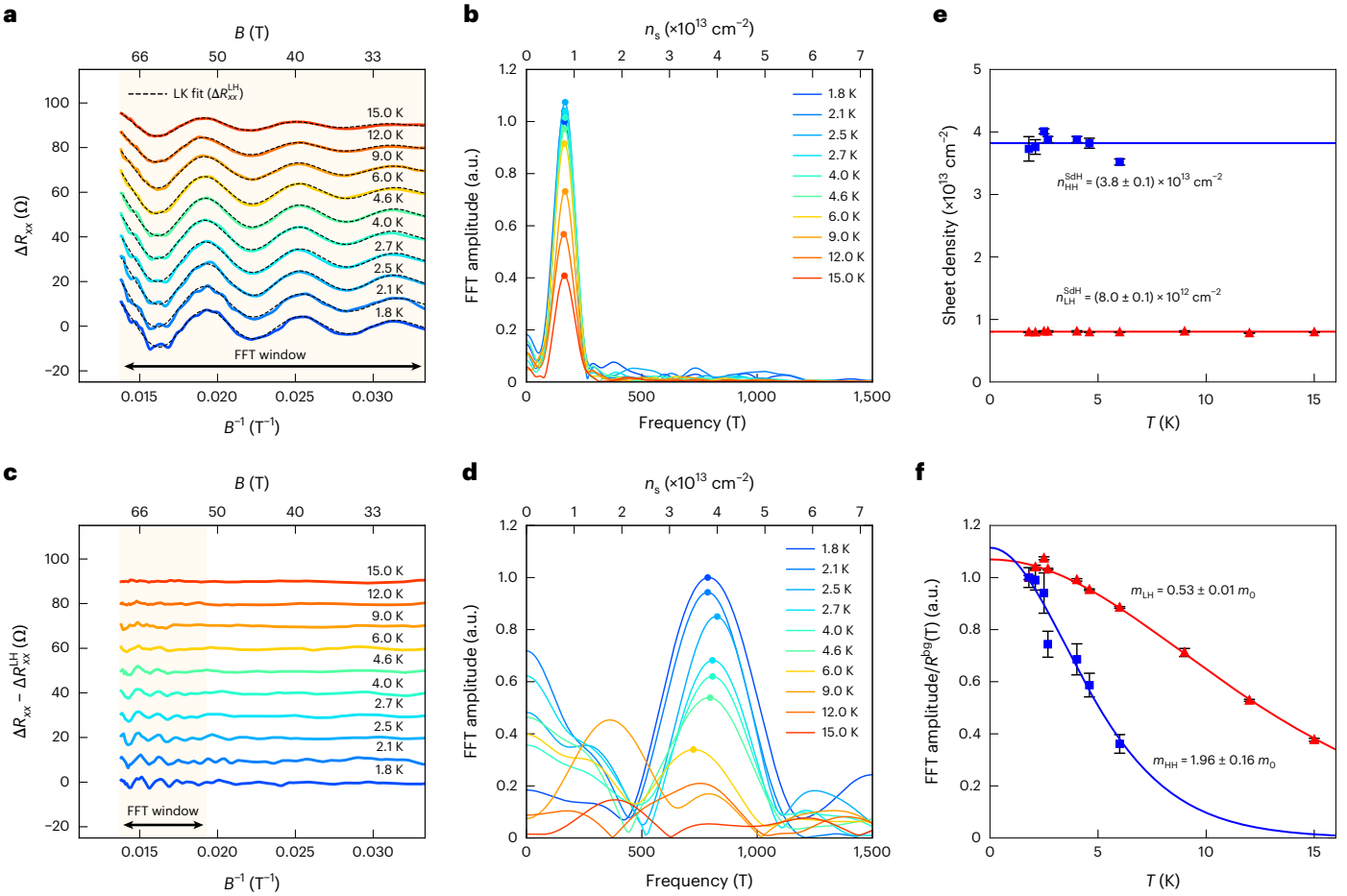

Fig. 2 | FFT analysis of SdH oscillations. a, Background-subtracted longitudinal resistance ΔR_{xx} plotted against 1/B, for temperatures from 1.8 K to 15 K. Dashed lines show least-square fits to the single-channel LK formula, performed separately at each temperature. **b**, FFT spectra of the data in **a**, taken in the indicated magnetic field window, normalized to the peak amplitude at 1.8 K. Peaks are indicated as solid circles; a dominant frequency peak at $f_1 \approx 166$ T is observed across all temperatures. **c**, Small-amplitude, high-frequency oscillations remaining after subtracting the LK fit from each curve in **a** (Supplementary Note II). **d**, FFT of the small-amplitude oscillations revealing a broader peak at $f_2 \approx 795$ T, well-resolved up to 6 K. A Hanning window is applied for the FFT spectra in **b** and **d** to suppress spectral leakage. Extended Data Fig. 5 shows the FFT spectra obtained using different windowing functions. **e**, Sheet density of LHs (triangles) and HHs (squares) obtained from oscillation frequencies. Solid lines and annotated densities represent the weighted average across temperatures. **f**, Temperature dependence of the FFT amplitude for LH and HH peaks, divided by the field-averaged background magnetoresistance (R_{xx}^{bg}; Methods and Extended Data Fig. 6) and normalized to the value at $T_0 = 1.8$ K. Solid lines are least-square fits to the thermal factor $\alpha\chi/\sinh(\chi)$ of the LK formula (Methods), yielding the annotated effective-mass values and standard error of the fits. In **e** and **f**, the plotted values and error bars represent the mean and standard deviation ($n = 5$) derived from five different FFT window functions (Extended Data Fig. 5).

HHs, and the underlying large-amplitude, low-frequency oscillations are due to the higher-mobility, lower-density LHs.

The Onsager relation relates each SdH oscillation frequency f to a corresponding Fermi surface[14]. Figure 2a shows ΔR_{xx}, which is periodic in $1/B$ and remains in phase across temperatures. Their fast Fourier transform (FFT) spectra in Fig. 2b show a dominant frequency peak at $f_1 \approx 166$ T observed across temperatures. The oscillatory resistance is fitted to the single-channel Lifshitz–Kosevich (LK) formula (Methods). A good fit (dashed lines in Fig. 2a) is obtained for the low-frequency, large-amplitude oscillations and subtracted out to retain only the high-frequency, small-amplitude oscillations (Fig. 2c). This subtraction effectively corresponds to a digital filter in the spectral domain that suppresses the fitted low-frequency signals (Methods and Supplementary Note II). The FFT spectra of the high-frequency oscillations are displayed in Fig. 2d, revealing a broader peak at $f_2 \approx 795$ T observed up to 6 K. Uncertainties in FFT peak frequencies and amplitudes are estimated by varying the window function used for FFT (Extended Data Fig. 5).

From the frequency of each oscillation component, a corresponding momentum-space Fermi surface area A can be calculated via the Onsager relation $A = (2\pi e/\hbar)f$. Then, an accurate measurement of sheet carrier density can be obtained via Luttinger's theorem, $n = 2A/(2\pi)^2$. For the low-frequency component (f_1), we obtain a sheet density $n_1^{SdH} = (8.0 \pm 0.1) \times 10^{12}\,cm^{-2}$, which is close to the LH density extracted from two-channel fitting in the Hall effect measurement $n_{LH}^{Hall} \approx 5 \times 10^{12}\,cm^{-2}$. The corresponding Fermi wavevector is $k_F^{(1)} = 0.709 \pm 0.004\,nm^{-1}$. The high-frequency oscillation component (f_2) has a corresponding sheet density of $n_2^{SdH} = (3.8 \pm 0.1) \times 10^{13}\,cm^{-2}$ and a Fermi wavevector of $k_F^{(2)} = 1.55 \pm 0.02\,nm^{-1}$. n_2^{SdH} is close to the HH density extracted from two-channel fitting, $n_{HH}^{Hall} \approx 5 \times 10^{13}\,cm^{-2}$. Consistent with polarization doping, no temperature dependence of n_1^{SdH} and n_2^{SdH} is observed from 1.8 K to 15 K where SdH is observed (Fig. 2e), as is the case for n_{LH}^{Hall} and n_{HH}^{Hall} from 2 K to 100 K where two-channel fitting can be applied (Extended Data Fig. 1).

With multiband conduction, it is preferable to separate SdH signals in each band based on σ_{xx} ($= R_{xx}/(R_{xx}^2 + R_{xy}^2)$) instead of the directly measured R_{xx}[32]. This procedure, however, requires also measuring the off-diagonal Hall resistance R_{xy} over the entire field and temperature range to invert the resistance tensor and obtain σ_{xx}. Although we did

https://doi.org/10.1038/s41928-026-01590-8

not record R_{xy} during the pulsed-field measurements, we compare SdH analyses of simulated σ_{xx} and R_{xx} as detailed in Supplementary Note II (equations and parameters relevant to the present sample are listed in Supplementary Tables 2 and 3). The simulated σ_{xx}, R_{xx}, $\Delta\sigma_{xx}$, ΔR_{xx} in single-band and two-band conduction scenarios are shown in Supplementary Fig. 2. We find that the analyses using these different quantities have no effect on extracted SdH oscillation frequencies (and hence the carrier densities) and, furthermore, relatively little effect on effective masses (Supplementary Fig. 3) and quantum mobilities (Supplementary Fig. 4). Informed by these simulations, we present the SdH analysis on the experimental measurements in this work based on R_{xx}.

Effective masses and quantum scattering times of HHs and LHs

The two distinct sets of oscillations from the LH and HH bands allow us to extract their effective masses. Figure 2f shows that the temperature dependence of the LH and HH FFT amplitudes, normalized by the non-oscillatory background magnetoresistance (Methods and Extended Data Fig. 6), is described accurately by the thermal damping term in the LK formula. We extract effective-mass values of 1.96 ± 0.16 m_0 for the HHs and 0.53 ± 0.01 m_0 for the LHs at their respective Fermi wave vectors, m_0 being the free electron mass. The larger mass of the HHs gives rise to a larger density of states (DOS) per unit area, consistent with their higher measured density, and a lower mobility, consistent with the larger magnetic field required to resolve their oscillations.

Reports of GaN hole mass in literature scatter from 0.3 m_0 to 2.2 m_0 (ref. 41), obtained by optical methods such as excitonic photoluminescence[42,43], optical reflectance[44] and spectroscopic ellipsometry[45,46] in which light-matter interaction couples the valence to the conduction band. SdH oscillations measure the valence (or conduction) band effective masses directly without the need to deconvolute the data because no interband coupling is required in this technique. In addition, SdH oscillations measure effective mass of carriers at the Fermi level (that is, at precise k-points), which can differ substantially from the zone-centre effective mass for high carrier concentration and non-parabolic bands.

Knowledge of the effective mass, along with the quantum mobility extracted from the field dependence of oscillation amplitude, gives the quantum scattering time τ_q, a measure of disorder broadening due to scattering from interface roughness, charged defects, and so on. We extract a quantum mobility μ_q = 382–413 cm^2 V^{-1} s^{-1} for the LHs at T = 1.8–15 K (Extended Data Fig. 7), consistent with the onset of oscillations at about 25 T. The corresponding τ_q for the LHs is ~0.13 ps. For the HHs, the relatively small signal-to-noise ratio of the oscillation amplitudes precludes a reliable extraction of μ_q using this method; instead, the onset of their oscillations in the approximate range of 50–60 T gives an estimated μ_q = 167–220 cm^2 V^{-1} s^{-1} for the HHs, corresponding to a τ_q of 0.17–0.24 ps. Both quantum mobilities are smaller than the Hall mobilities, with a μ_{Hall}/μ_q ratio of around 5 for the LHs and around 2–2.5 for the HHs. A ratio close to unity is obtained for short-range, isotropic scattering mechanisms, such as interface roughness scattering. A ratio much larger than unity is obtained for long-range scattering mechanisms that favour small-angle scattering, such as remote ionized impurity scattering[47]. For the ratios obtained here of around 2–5, it is unclear at this stage which extrinsic scattering mechanism dominates.

Comparison with theory and a larger-than-predicted LH mass

We now compare the hole masses extracted from the quantum oscillations with those derived from the six-band $k{\cdot}p$ method[48,49] and the ab initio GW method (Methods). Figure 3a shows the in-plane dispersions $E(k)$ of the HHs and LHs. For the $k{\cdot}p$ method, quantum confinement in the GaN/AlN QW is accounted for, and the energy dispersions shown are the first HH and LH subbands of the QW. The first split-off (SO) subband lies deeper than 300 meV from the VBM. Separately, we compute the ab initio band dispersions of a strained bulk GaN crystal (solid lines in Fig. 3a). In the energy window between 0 meV and 150 meV, a good agreement between the two methods is obtained.

From the dispersions, we compute the cyclotron effective mass, $m_{CR} = \hbar^2 k(\partial E/\partial k)^{-1}$ (Fig. 3c,d) and the DOS per unit area, $m_{CR}/\pi\hbar^2$ (Fig. 3b). Both methods indicate mixing of the LH and HH states near the zone centre (k = 0 nm^{-1}), where the LHs and HHs share a common effective mass of 0.45 m_0. Away from the zone centre, they recover their individual masses: 1.6–2.1 m_0 for HH and 0.29 m_0 for LH. As shown in Fig. 3c, although the measured HH mass of 1.96 ± 0.16 m_0 is in good agreement with both theoretical methods, the measured LH mass of 0.53 ± 0.01 m_0 is substantially larger. In the following, we investigate the field dependence of the LH mass in light of this discrepancy.

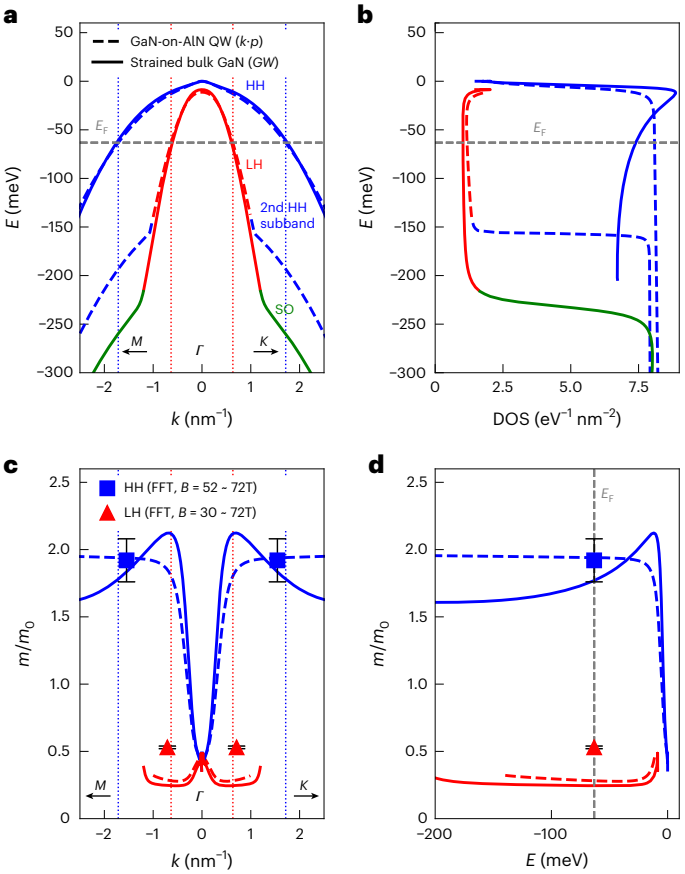

Fig. 3 | Calculated band dispersions and effective masses. a, HH and LH dispersions in the plane of the 2DHG (perpendicular to the c axis of the wurtzite crystal) calculated using the $k{\cdot}p$ method for a GaN/AlN QW (dashed curves) and using first-principle GW calculations for a GaN bulk crystal fully strained to AlN (solid curves). k = 0 is Γ point (zone centre); k < 0 is the Γ → M direction, and k > 0 is the Γ → K direction. The horizontal dashed line is the Fermi level determined from a self-consistent $k{\cdot}p$–Poisson calculation assuming a surface Fermi level at 1.9 eV above the VBM. The vertical dashed lines indicate the Fermi wave vector of the LHs and HHs. **b**, DOS per unit area of the LH and HH bands as a function of energy. **c**,**d**, Cyclotron effective masses (Methods) of the LHs and HHs, calculated from the dispersions in **a**, as a function of in-plane wave vector (**c**) and energy (**d**). The cyclotron effective mass m is directly related to the 2D DOS per unit area via DOS = $m/\pi\hbar^2$. The measured HH and LH masses determined from fits to the FFT amplitudes (Fig. 2f) are shown as squares and triangles, respectively, where their centre values and error bars indicate the mean and standard deviation when using five different FFT window functions (caption of Fig. 2). In **c**, the Fermi wave vectors of the experimental data points are calculated from the measured densities n as $k_F = \sqrt{2\pi n}$. SO, split-off.

https://doi.org/10.1038/s41928-026-01590-8

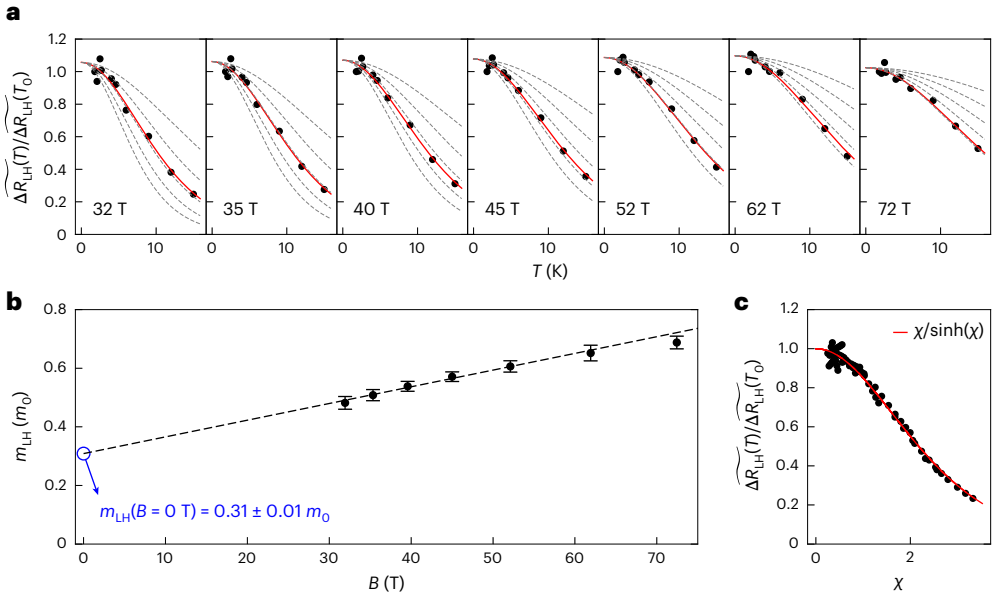

Fig. 4 | Field dependence of LH mass. a, Normalized oscillation amplitude taken from the fitted dashed lines in Fig. 2a at various magnetic fields. $\widetilde{\Delta R_{LH}} = \Delta R_{LH}/R_{xx}^{bg}(T, B)$ is the background-normalized (Methods) LH oscillation amplitude, and $T_0 = 1.8$ K is the base temperature. At each field, the effective mass is independently obtained by fitting to the $\alpha\chi/\sinh(\chi)$ term of the LK formula, where α is a constant prefactor and $\chi = 2\pi^2 k_B T/[\hbar\omega_c(B)]$. The grey dashed lines show the LK curves for 0.3–0.7 m_0 from top to bottom in increments of 0.1 m_0. **b**, LH effective mass m_{LH} as a function of magnetic field linear increase from 0.48 ± 0.01 m_0 at $B = 32$ T to 0.68 ± 0.02 m_0 at $B = 72$ T. The dashed line is a linear fit that extrapolates to 0.31 ± 0.01 m_0 at $B = 0$ T. All uncertainties, including in the extrapolated intercept, represent best-fit values ± standard error of the respective fit. **c**, The same data as in **a**, scaled by the fitted α and plotted against χ. Each data point's corresponding B and m_{LH} (from **b**) are used to compute $\omega_c(B) = eB/m_{LH}$. This scaling shows that all of the data points in **a** (taken at different B and yielding different m_{LH}) are all well-described by the LK formula.

Anomalous field dependence of the LH effective mass

The high magnetic field available in this study and the large signal-to-noise ratio of the LH oscillations enabled us to perform an LK fit for each LH oscillation peak (Fig. 4a) to extract the LH mass as a function of field. Surprisingly, we observe a linear increase in the LH mass from 0.48 m_0 at 32 T to 0.69 m_0 at 72 T (Fig. 4b), with the field-averaged value of 0.53 m_0 extracted from FFT amplitudes falling in this range. The oscillation amplitudes at different magnetic fields (Fig. 4a) can be collectively plotted against $\chi = 2\pi^2 k_B T/[\hbar\omega_c(B)]$ as shown in Fig. 4c, confirming the robustness of the LK fit across temperatures and magnetic fields[16]. Extrapolating to $B = 0$ T, we obtain a mass of 0.31 m_0, which is close to the theoretical value.

The same linear field dependence and extrapolated zero-field mass of around 0.3 m_0 are reproduced on a different sample measured up to 58 T (Extended Data Fig. 8). We currently do not have a clear justification for the linear extrapolation and the origin of the magnetic field dependence of the LH mass. A field-dependent effective mass as measured by SdH oscillations has been reported in several materials[21–26,50,51]. A linear dependence of the electron mass on magnetic field has been reported in AlGaN/GaN 2DEG heterostructures and attributed to conduction band non-parabolicity[21–23]. We investigated the effects of non-parabolicity by calculating the LH and HH LLs from their non-parabolic dispersions (Methods). We find that, for both LH and HH, the LLs near the Fermi level are evenly spaced and have approximately equal cyclotron effective masses even out to $B = 32$ T and $B = 72$ T (Extended Data Fig. 9). Consistently, the LH oscillation period shows no field dependence (Fig. 2a). Thus, non-parabolicity alone is unable to explain the observed field dependence of the LH mass. A field-dependent effective mass has also been observed for holes in similarly asymmetric GaAs/AlGaAs heterostructures, with its origin left unexplained[24,25], as well as for electrons in a symmetric double QW with its origin attributed to electron–electron interaction[26].

We mentioned earlier that with multiband conduction, it is preferable to separate SdH signals in each band based on σ_{xx} instead of R_{xx} (ref. 32). However, our simulation results (Supplementary Note II) show that the observed B-dependent effective mass cannot be traced simply to the SdH analysis based on R_{xx}. On the other hand, it is worth noting that, if not correctly accounted for, a strong temperature dependence of the non-oscillatory background magnetoresistance (R_{xx}^{bg}) could give rise to systematic error in the LK analysis of $\Delta R_{xx}/R_{xx}^{bg}$, including incorrectly suggesting a field-dependent effective mass. We have made independent DC-current measurements of R_{xx}^{bg} to mitigate this potential artefact (Methods and Extended Data Fig. 6). We emphasize that the field-dependent mass is a robust feature beyond random error in the background normalization and is reproducible in another sample; however, we cannot fully rule out additional unknown systematic errors. Further experiments and theory are necessary to corroborate our observed trend and elucidate its origin.

Conclusions

Using polarization doping to generate mobile holes that survive at cryogenic temperatures, combined with sharp and clean GaN/AlN interfaces grown by MBE, we measure—by Hall effect—mobilities of around 2,000 $cm^2 V^{-1} s^{-1}$ for LHs and 400 $cm^2 V^{-1} s^{-1}$ for HHs at 2 K. Subsequently, we observe distinct quantum oscillations of LHs and HHs in GaN and obtain their respective sheet densities, quantum scattering times and effective masses. Mobilities above 1,400 $cm^2 V^{-1} s^{-1}$ for LHs and above 300 $cm^2 V^{-1} s^{-1}$ for HHs at cryogenic temperatures have also been measured across multiple samples (Extended Data Fig. 8 and ref. 40), attesting to the robustness of these polarization-doped heterostructures.

The effective-mass measurements provide critical parameters for device design and are valid at all temperatures. Furthermore, the design of GaN p-channel field-effect transistors must account for the parallel HH–LH conduction described in this work. Another application of interest is cryogenic GaN CMOS operating near 5 V, which could facilitate compact and simple designs for control electronics serving quantum

technologies. The relatively high hole mobilities achieved at cryogenic temperatures suggest a viable route towards high-speed p-channel field-effect transistors in GaN and, subsequently, high-performance cryogenic GaN CMOS.

The ability to directly probe the valence bands of GaN via quantum oscillations provides a route to more fundamental studies of this important semiconductor family. Of immediate interest is the response of the valence bands to applied strain, with the goal of lowering the hole effective mass and boosting hole mobility[6,7], a strategy already employed in commercial p-type silicon transistors. Strain-engineered p-GaN is essential to close the performance gap between p- and n-channel GaN transistors, a prerequisite for realizing well-balanced GaN CMOS at room temperature.

The LHs reported in this study have a low density of ~8×10^{12} cm^{-2}, such that the Fermi level populates only four LLs at $B = 72$ T (filling factor $\nu = 4$). Reducing the LH density by gating or by decreasing the GaN layer thickness can push the 2DHG towards $\nu = 1$ at accessible magnetic fields. Along with further improvements in mobility, a lower-density 2DHG may bring the integer and fractional quantum Hall regimes within reach. Such experiments offer an interesting platform for studying quantum Hall physics due to the strong coupling of GaN holes to acoustic phonons[6,7], interaction between HHs and LHs and a larger Fermi surface than that of conventional 2D systems. The strong hole–acoustic phonon coupling and the large DOS provided by the large HH mass may be of interest in exploring superconductivity in this material platform.

The use of polarization-induced doping to enable quantum oscillation could be applied to other wide-bandgap semiconductors in which other methods to create mobile carriers are problematic. For example, in ZnO/MgZnO heterostructures, polarization-doped 2DEGs with mobility >10^6 cm^2 V^{-1} s^{-1} have enabled SdH studies of quantum scattering times[52] and spin–orbit coupling[53] and have entered the integer and fractional Hall regimes[15,54,55]. For SiC, polarization-doped 2DEG in a 3C/4H-SiC heterostructure has enabled an electron mobility >7,000 cm^2 V^{-1} s^{-1} at 32 K (ref. 56), and quantum oscillations studies are potentially within reach. For both wide-bandgap ZnO and SiC, the p-type dual—the 2DHG—remains to be confirmed. As in GaN, improvements in impurity control[36] and epitaxial growth[35] could lead to high-mobility, uncompensated 2DHG by polarization doping, which would, in turn, allow quantum oscillation studies to reveal new information about these wide-bandgap semiconductor families.

Note added in proof: During typesetting of this article, the GaN/AlN heterostructure with a high-mobility 2DHG grown in our laboratory has also enabled the observation of cyclotron resonance and subsequent extraction of HH and LH cyclotron masses and mobilities[57].

Methods

Sample preparation

GaN/AlN heterostructures were epitaxially grown in a Veeco Gen10 MBE system. Metal (Al, Ga, Mg) fluxes were provided by effusion cells containing high-purity elemental sources. Active nitrogen flux was provided by high-purity N_2 gas flowing at a rate of 0.3 sccm through a radio frequency plasma source operating at a power of 400 W. The resulting growth rate was 0.21 μm h^{-1} for all layers in the heterostructure. In situ monitoring of film growth was performed using reflection high-energy electron diffraction apparatus by KSA Instruments with a Staib electron gun operating at 14.5 kV and 1.45 A. The single-crystal, Al-polar AlN substrates used in this study were from Crystal IS and have dislocation density <10^4 cm^{-2} (ref. 37). The substrates were initially cleaned ex situ by solvents (acetone, isopropanol), acids (phosphoric acid, sulfuric acid and hydrofluoric acid) and de-ionized water, as outlined in our previous works[38,39]. They were then mounted on faceplates and loaded into the load-lock chamber of the MBE system, where they were outgassed at 200 °C for 7 h. Before the epitaxial growth, the substrates were cleaned in situ by repeated cycles of Al adsorption and desorption to remove native surface oxide[38,39]. A 500-nm AlN buffer layer was grown under Al-rich conditions at a thermocouple temperature of T_{TC} = 1,060 °C, after which excess Al was thermally desorbed at T_{TC} = 1,100 °C for 45 min. Then, ten periods of thin $Al_{0.95}Ga_{0.05}N$ layers (2–3 monolayers in each), separated by 25-nm AlN spacers, were grown at T_{TC} = 875 °C. These layers serve to prevent n-type silicon impurities floating on the growth front during AlN buffer growth from reaching the GaN/AlN interface and compensating the 2DHG[36]. The substrate was cooled to T_{TC} = 835 °C before starting GaN growth. Then, the 15-nm GaN layer was grown, with the topmost 5.5 nm heavily doped with Mg with concentration ~5×10^{19} cm^{-3}, based on a calibration growth where a series of GaN:Mg layers were grown by varying Mg cell temperatures and the Mg concentrations were determined by secondary ion mass spectrometry measurement. This GaN:Mg layer enables low-resistance metal contacts with the 2DHG by decreasing the potential barrier width through which holes are injected from the metal contacts. Before this growth step, the Mg source shutter was kept closed. Note that due to the large thermal activation energy of the Mg acceptor (~170 meV) and surface charge depletion, the total sheet hole density in the 5.5-nm Mg-doped top layer remains below 1×10^9 cm^{-2} even at 300 K (k_BT = 26 meV) and is nominally zero at 1.8 K (k_BT = 0.16 meV), according to Schrödinger–Poisson simulation (Fig. 1c). Parallel conduction in the Mg-doped GaN layer during transport measurements was therefore negligible. After epitaxial growth, the substrates were immediately cooled to room temperature, and excess Ga droplets remaining on the surface were removed by HCl after the sample was unloaded from the MBE system.

Mesa isolation of the Hall bar was first performed by a BCl_3 inductively coupled plasma etch into the AlN substrate through a photoresist mask (SPR 770). Following photolithography, HCl and HF dip, Ni/Au contacts (15/20 nm) were deposited by electron-beam evaporation (~3×10^{-6} Torr pressure and 0.1 nm s^{-1} deposition rate) and, following metal lift-off, annealed at 450 °C in O_2 for 60 s. Finally, a Ti/Au (15/250 nm) stack was electron-beam evaporated to thicken the contact pads where electrical leads were to be attached. A photograph of a fabricated Hall bar is displayed in Extended Data Fig. 2 along with its dimensions.

Magnetotransport measurement

Low-field (−9 T to +9 T) magnetotransport measurements were performed on the fabricated Hall bars in a Dynacool physical property measurement system system from Quantum Design using the standard six-probe technique with a DC excitation current of 50 μA. Longitudinal (R_{xx}) and Hall (R_{Hall} or R_{xy}) resistances were symmetrized and antisymmetrized, respectively, in a magnetic field.

Pulsed-field measurements were performed in the 75-T Duplex magnet at the National High Magnetic Field Laboratory Pulsed Field Facility at Los Alamos National Laboratory. Temperatures down to 1.8 K were obtained using a ^{4}He cryostat with samples immersed in superfluid ^{4}He for optimal heatsinking. Copper wires were attached to the Ni/Au contact pads of the Hall bar using silver epoxy and secured using GE varnish to minimize mechanical vibrations during pulsed-field measurements. To minimize induced voltages produced by the pulsed field, care was taken to minimize any open-loop area formed by the copper wires (Extended Data Fig. 2a), and only R_{xx} was measured on the Hall bar to ensure the highest signal-to-noise for R_{xx}.

Four-probe measurements of R_{xx} were performed using a lock-in method, wherein the applied current was modulated sinusoidally at 40 kHz with a root-mean-square (RMS) amplitude of 50 μA. The induced voltage was therefore also sinusoidally modulated and was detected with fast digitizers. The lock-in frequency was chosen to be 40 kHz by observing the field profile (B versus time) shown in the inset of Extended Data Fig. 3a. When the inner coil of the duplex magnet fires and boosts the field from 25 T to 72 T, the sweep rate is approximately 20 T ms^{-1}. A lock-in frequency of 40 kHz (period of 0.025 ms) ensures approximately one lock-in cycle per 0.5 T.

The in-phase and out-of-phase (quadrature) components of the measured voltage were determined offline using a software implementation of a lock-in amplifier (which isolates the detected voltage response at 40 kHz and filters away noise at other frequencies). The phase factor used for lock-in processing was chosen to give maximum SdH oscillation amplitudes in the in-phase component of the measured voltage, which was then used to obtain R_{xx}. We found that the oscillation amplitudes are nearly independent of the phase factor in a ±10° window. Even though the out-of-phase component cannot be completely removed at all fields due to the high modulation frequency and the finite resistance-capacitance (RC) time constant across the sample, such a choice of phase factor always makes the out-of-phase component featureless: that is, containing no oscillatory signals and flat with magnetic field.

The time constant used for digital lock-in processing was fixed at 250 µs, which was ten times the period of current modulation. All data presented in this work did not undergo additional smoothing (for example, low-pass or Savitzky–Golay filtering), which may artificially dampen oscillations.

Extended Data Fig. 3a shows the R_{xx} data recorded during the rising-field (0 → 72 T, dashed curves) and falling-field (72 → 0 T, solid curves) portions of the pulsed-field measurements (the field sweep profile is shown in the inset). The hysteresis between the rising-field and falling-field data is small, and we used the falling-field data due to slightly superior data quality.

To assess whether the magnitude of AC current used (50 µA RMS) was appreciably heating the sample, we used the LH and HH oscillation amplitude as a relative probe of sample temperature. Extended Data Fig. 3b–e shows the falling-field data at two temperatures where both LH and HH oscillations are clearly resolved, measured with AC currents with 50 µA and 25 µA RMS values. We did not observe a noticeable difference in LH and HH oscillation amplitudes at these two currents despite a fourfold difference in injected power ($P = I^2R$). We therefore concluded that sample heating by current flow was not pronounced at 50 µA RMS AC current.

SdH signal processing and spectral analysis

As described in Supplementary Note II, $R_{xx}(B)$ in this work contains the following three components, which, when plotted as a function of $1/B$, occur at different frequencies:

(1) A slowly varying (low-frequency) 'polynomial' background, due to non-SdH physics
(2) A small oscillatory component at intermediate frequency, due to LH SdH oscillations
(3) A smaller-amplitude oscillatory component at high frequency, due to HH SdH oscillations

The filtering of component 1 from the total signal to reveal components 2 and 3 and the filtering of component 2 to reveal component 3 can be accomplished purely via spectral analysis of the signal by taking the Fourier transform of the total signal (aided by appropriate use of windows centred on the parts of the signal where the oscillations occur).

Alternatively, to improve signal-to-noise in the spectral domain, the same filtering can be equivalently achieved by first fitting and subtracting the slowly varying component 1 from the raw data to more clearly reveal the higher-frequency oscillatory components 2 and 3, as shown in Extended Data Fig. 4, where a fifth-order polynomial is used to fit the background resistance (see also Supplementary Fig. 1 and Supplementary Table 1 on the use of other polynomial orders). Effectively, this corresponds to a digital filter in the spectral domain that suppresses low-frequency signals.

Similarly, to more clearly reveal the high-frequency HH oscillations, the well-behaved intermediate-frequency LH oscillations can be fitted to the single-channel LK equation (dashed curves in Fig. 2a) and then subtracted to obtain only the HH oscillations (Fig. 2c). The same filtering can be achieved purely via spectral analysis (that is, by directly applying a localized window function covering only the high-B-field region where HH oscillations are visible). We analysed our data using both approaches, and the measured amplitudes of the HH and LH oscillations (and their dependence on temperature, yielding mass) were unaffected, with the subtraction method giving improved signal-to-noise in the resulting HH peak. The use of R_{xx} instead of the longitudinal conductivity σ_{xx} is discussed in Supplementary Note II.

FFT was used to determine the oscillation frequencies of the LHs and HHs and their field-averaged amplitudes. The finite magnetic field window in which FFT is performed leads to spectral leakage in the resulting spectrum, which was mitigated by multiplying the data with a window function before FFT. The resulting spectrum may depend on the specific window chosen. Extended Data Fig. 5 shows FFT spectra obtained when using different window functions. The error bars in Fig. 2e,f reflect the spread (one standard deviation) in FFT peak frequencies and amplitudes when different window functions are applied.

SdH analysis of σ_{xx} and R_{xx} using simulation can be found in Supplementary Note II with equations and parameters relevant to the present sample.

Background magnetoresistance

The non-oscillatory background resistance (component 1) originates from the magnetoresistance of the sample; however, when measured at relatively high frequencies (in this case, 40 kHz), this background can become distorted owing to the changes in the RC time constant of the measurement when the total resistance (sample and contacts) changes with magnetic field.

Although DC-current measurements performed in a physical property measurement system consistently show a positive-slope magnetoresistance in $R_{xx}(B)$ across the accessible field range of $B = -9$ T to +9 T, the polynomial-fitted background resistance $R_{xx}^{\mathrm{AC,bg}}(B)$ determined from AC current measurement (Extended Data Figs. 3a and 4a) shows a negative slope in magnetoresistance, which is an artefact of the RC time constant of the circuit and the high lock-in frequency required for pulsed-field measurements. It was found to be dependent on the pulsed magnet used and the electrical leads attached to the sample. For instance, on the other sample shown in Extended Data Fig. 8 with different electrical leads attachment and measurement conditions, the AC-background magnetoresistance $R_{xx}^{\mathrm{AC,bg}}(B)$ shows a positive slope.

Strictly speaking, normalization of the oscillation amplitude ΔR_{xx} by the true background magnetoresistance R_{xx}^{bg} is required before using the LK formula to fit $\Delta R_{xx}/R_{xx}^{\mathrm{bg}}$ versus temperature and extract effective mass. Here we approximated the true $R_{xx}^{\mathrm{bg}}(B)$ with $R_{xx}(B)$ measured with DC injection current—$R_{xx}^{\mathrm{DC}}(B)$—under pulsed magnetic field up to 72 T at T = 1.4 K and T = 17 K (Extended Data Fig. 6). At each temperature, two pulsed measurements were collected with opposite field directions, and their falling-field curves were averaged ('symmetrized'). DC measurements in a pulsed-field environment are inherently noisier, particularly when two datasets (opposite field directions) are averaged, leading to washed-out, unresolved SdH oscillations. Nevertheless, these measurements were performed only to approximate R_{xx}^{bg} and check its temperature dependence. A simple linear interpolation was used to approximate $R_{xx}^{\mathrm{bg}}(\mathrm{B,T})$ at intermediate temperatures between 1.4 K and 17 K. The same $R_{xx}^{\mathrm{bg}}(\mathrm{B,T})$ data shown in Extended Data Fig. 6 were also applied to the analysis on the other similar sample shown in Extended Data Fig. 8.

It is worth noting that if the measured R_{xx}^{DC} somehow deviates substantially from the true R_{xx}^{bg}, it is possible for an apparent B-dependent mass to manifest as an artefact even if the true effective mass is independent of B.

Simulation

Energy-band diagrams and band dispersions of the QW heterostructure were simulated by self-consistently solving the six-band $k{\cdot}p$ equation[48]

with the Poisson equation using the commercial software nextnano[58]. At the top GaN surface, the Fermi level was assumed to lie 1.9 eV above the VBM (ϕ_B = 1.9 eV) according to electroreflectance experiments on a similar MBE-grown GaN/AlN structure[59]. Nevertheless, the position of the Fermi level in the QW is relatively insensitive to the Fermi level at the surface, varying by less than ±1 meV when ϕ_B is varied by ±0.2 eV.

The Rashba–Sheka–Pikus parameters (A_{1-6}) and the deformation potentials ($a_{cz} - D_1$, $a_{ct} - D_2$, D_{3-6}) were taken from ref. 60 and ref. 61, respectively. In addition, Burt's exact envelope function theory[49,62] was used to generalize the $k{\cdot}p$ method to heterostructures and obtain the band structures for the quantum-confined 2DHG in a strained GaN/AlN QW. The spontaneous polarization constants P_{sp} and piezoelectric polarization constants e_{33}, e_{31}, e_{51} were taken from ref. 63. Other material parameters were taken from ref. 64. All relevant input parameters used in $k{\cdot}p$–Poisson calculations are listed in Extended Data Table 1.

Ab initio band-structure calculations of strained bulk GaN were performed within the framework of density functional theory and *GW* perturbation theory using the Quantum ESPRESSO package[65] and the BerkeleyGW code[66]. The Wannier90 code[67] was utilized to interpolate *GW* quasiparticle energy. The local density approximation to the exchange and correlation functional was used[68], and the spin–orbit coupling was included through fully relativistic optimized norm-conserving Vanderbilt pseudopotentials[69]. To increase accuracy, we included Ga semicore states in the pseudopotential. A plane-wave kinetic energy cutoff of 180 Ry was used for Kohn–Sham wavefunctions. The Brillouin zone was sampled on a 10 × 10 × 10 Γ-centred k-mesh. The effect of strain due to growth on the substrate AlN was considered by epitaxially straining bulk GaN to the lattice of AlN in the basal plane. We used the experimental lattice constants of GaN and AlN instead of ab initio values[60]. We performed one-shot *GW* calculations to obtain the quasiparticle renormalization of band energies[70]. We used 800 spinor states to converge quasiparticle eigenvalue corrections and a kinetic energy cutoff of 15 Ry for the dielectric matrix. Both density functional theory and *GW* eigenvalues were averaged over spin doublets, and axial symmetry around z was imposed to obtain isotropic dispersions in the plane. For the Wannier interpolations of *GW* eigenvalues, maximally localized Wannier functions were obtained from N-2p initial projections for the 12 spinor bands in the highest disentangled valence band manifold, and the coarse grid was also a 10 × 10 × 10 Γ-centred k-mesh.

TEM

Cross-section lamella of a representative GaN/AlN heterostructure sample was prepared using a Thermo Fisher Helios G4 UX Focused Ion Beam. The lamella was prepared using a gallium focused ion beam at 30 keV for the bulk milling step and 5 keV for the final milling step to reduce damage. STEM measurements were taken with an aberration-corrected Thermo Fisher Spectra 300 CFEG operated at 300 keV.

Definition of cyclotron mass

In the semiclassical description, an external magnetic field leads to orbital motion of electrons in both real and momentum space in the plane perpendicular to the external field. For electrons occupying different available energy levels, the field causes electrons to orbit on different loci of constant energy in momentum space. The enclosed momentum-space area A is a function of energy and, via the dispersion relation $E(k)$, also a function of the wave vector k. For each orbit, the angular frequency is $\omega_c = eB/m_{CR}$, where the cyclotron effective mass m_{CR} is defined as

$$m_{CR} \equiv \frac{\hbar^2}{2\pi}\frac{\partial A(E)}{\partial E} = \frac{\hbar^2}{2\pi}\frac{\partial A}{\partial k}\left(\frac{\partial E}{\partial k}\right)^{-1}.$$

For a 2D system that is approximately isotropic in the plane perpendicular to the magnetic field, the Fermi surface is circular with area $A = \pi k^2$, and m_{CR} becomes

$$m_{CR}(k) = \hbar^2 k\left(\frac{\partial E}{\partial k}\right)^{-1}.$$

The cyclotron mass is related to the first derivative of $E(k)$ and is directly related to the 2D DOS per unit area DOS(E) via

$$\mathrm{DOS}(E) = \frac{m_{CR}(E)}{\pi\hbar^2}.$$

If $E(k)$ is parabolic in some region of k (that is, locally well-described by $E(k) = \hbar^2k^2/2\tilde{m}$), then m_{CR} is equal to the 'curvature' effective mass $m_{curv} = \hbar^2\left(\frac{\partial^2 E}{\partial k^2}\right)^{-1}$: that is, $m_{CR} = m_{curv} = \tilde{m}$.

LLs for non-parabolic dispersions

In the quantum mechanical description of cyclotron motion[14], the Bohr–Sommerfeld rule leads to a quantization of the real-space area of cyclotron orbits such that they contain integer multiples of the flux quantum, $\phi_0 = \hbar/e$. The momentum-space area is also quantized as

$$A_n = \left(n + \frac{1}{2}\right)\frac{2\pi eB}{\hbar} = A_n(B),\ n = 0, 1, 2, \ldots$$

For a circular Fermi surface where $A = \pi k^2$, a quantization of the momentum-space area implies a quantization of allowed wave vectors

$$k_n(B) = \sqrt{\frac{A_n(B)}{\pi}} = \sqrt{\left(n + \frac{1}{2}\right)\frac{2eB}{\hbar}},\ n = 0, 1, 2, \ldots$$

which in turn leads to quantized energy levels. Lifting of spin degeneracy by Zeeman effect would split each n into two levels, $n\uparrow$ and $n\downarrow$. Each $n\uparrow\downarrow$ corresponds to a LL, labelled N in Extended Data Fig. 9. Note that contrary to the common derivation of LLs by the replacement $\mathbf{p} \rightarrow \mathbf{p} + e\mathbf{A}$ in an effective-mass Hamiltonian, this derivation does not require the assumption of a parabolic dispersion. Consequently, the LLs may not be equally spaced in the case of non-parabolic dispersions. The LLs are obtained by first calculating the quantized wave vectors and then calculating their corresponding energies from the dispersion. Furthermore, each LL may have a different cyclotron frequency and cyclotron mass. This calculation is illustrated in Extended Data Fig. 9 for B = 32 T and B = 72 T, neglecting Zeeman splitting so that each of the plotted energy levels (horizontal lines) contains two spin-degenerate LLs. At B = 32 T, eight LH LLs are occupied; at B = 72 T, four LH LLs are occupied. Non-parabolicity of the LH and HH bands is captured by the nonlinearity of the LLs as a function of magnetic field, most evident in low fields (Extended Data Fig. 9e).

For electrical transport, especially at cryogenic temperatures, only charge carriers near E_F are relevant. Despite the non-parabolicity of both bands, the cyclotron masses of the LLs in the vicinity of E_F are approximately constant (0.28–0.29 m_0 for LHs and 1.94 m_0 for HHs) at both B = 32 T and B = 72 T. Consistently, the LLs for both the LHs and HHs are approximately equally spaced near E_F and are linear in magnetic field: that is,

$$E_n(B) \approx \hbar\frac{eB}{m_{CR}^{E_F}}\left(n + \frac{1}{2}\right)$$

where $m_{CR}^{E_F}$ is the cyclotron mass of the LLs near E_F. Therefore, the measured oscillation frequency or period should show no field dependence—as verified in Fig. 2a.

The LK formalism for quantum oscillations

When the Fermi level (defined here to be synonymous with the chemical potential) is approximately fixed in an experiment, the DOS at E_F oscillates with increasing magnetic field as the LLs move away from each other. Quantities that depend on the DOS at E_F, including electrical

resistance, will thus oscillate accordingly. The oscillation amplitude depends on the magnitude of change of the DOS at E_F as a function of magnetic field, dampened by the finite width of the LLs and the finite sharpness of the Fermi–Dirac distribution around E_F. In the LK formalism[14], the oscillatory component of longitudinal resistance (R_{xx}) has the form

$$\Delta R_{xx} = CR_D R_T \cos\left(2\pi f \frac{1}{B}\right)$$

$$R_D = \exp\left(-\frac{\pi}{\omega_c^{E_F}\tau_q}\right) = \exp\left(-\frac{\pi}{\mu_q B}\right)$$

$$R_T \equiv \frac{\chi}{\sinh\chi}$$

where C is an amplitude prefactor, f is the oscillation frequency in B^{-1}, $\omega_c^{E_F} = eB/m_{CR}^{E_F}$ is the cyclotron frequency of the LLs near E_F, τ_q is the quantum scattering time, $\mu_q = e\tau_q/m_{CR}^{E_F}$ is the quantum mobility and $\chi = 2\pi^2\left[k_B T/\hbar\omega_c^{E_F}(B)\right]$. See Supplementary Note II for more details on the case of multiband conduction and oscillations in the conductivity tensor.

The Onsager relation[14] relates f to the momentum-space area via $A = (2\pi e/\hbar)f$. For an isotropic dispersion with a circular Fermi surface, A is then related to the carrier sheet density n via Luttinger's theorem, $n = 2A/(2\pi)^2$, where the factor of 2 accounts for spin degeneracy. A direct measurement of the sheet density can thus be obtained via $n = (2e/h)f$, where h is Planck's constant. The Dingle factor R_D describes the reduction of oscillation amplitude by disorder, which for a scattering time of τ_q leads to a broadening of the LLs by $\hbar/\tau_q$ via the uncertainty principle. This disorder damping of the oscillation amplitude is especially severe if the LLs are closely spaced near E_F, that is, when $\hbar\omega_c^{E_F}$ is small due to a large $m_{CR}^{E_F}$ or small B—thus the dependence on $\omega_c^{E_F}$ in the Dingle factor. Similarly, the thermal damping factor R_T describes the reduction of oscillation amplitude due to the broadening of the Fermi–Dirac distribution around E_F at finite temperatures. This reduction is a function of the ratio of thermal energy $k_B T$ to the spacing between LLs near E_F, $\hbar\omega_c^{E_F}$.

As shown in the previous section, despite the non-parabolicity of the bands, the cyclotron masses of the LLs nearest to E_F are approximately constant (equal to a single value of $m_{CR}^{E_F}$), and the LLs are approximately equally spaced by $\hbar\omega_c^{E_F}$. To determine $m_{CR}^{E_F}$, the standard procedure is to analyse the temperature dependence of the oscillation amplitude at a particular field. The standard approach is to first normalize the amplitudes by the amplitude at the lowest measured temperature and then fit the temperature dependence to $\chi/\sinh(\chi)$ with $m_{CR}^{E_F}$ as the only fitting parameter. Because $\chi/\sinh(\chi)$ approaches unity at $T = 0$ K, this approach makes the implicit assumption that the lowest temperature is sufficiently low that the measured amplitude approaches the $T = 0$ K limit. This assumption can be removed by fitting instead to $\alpha\chi/\sinh(\chi)$, where α is a constant fit parameter greater than unity. When fitting FFT amplitude, the value of B used in the expressions of ω_c and χ is based on the harmonic mean B^* of the FFT window: $\frac{1}{B^*} = \frac{1}{2}\left(\frac{1}{B_{min}} + \frac{1}{B_{max}}\right)$.

Data availability

Source data that support the findings of this study are available from the corresponding authors upon reasonable request.

References

1. Amano, H. Nobel lecture: growth of GaN on sapphire via low-temperature deposited buffer layer and realization of p-type GaN by Mg doping followed by low-energy electron beam irradiation. *Rev. Mod. Phys.* **87**, 1133–1138 (2015).
2. Amano, H. et al. The 2018 GaN power electronics roadmap. *J. Phys. D Appl. Phys.* **51**, 163001 (2018).
3. Hoo Teo, K. et al. Emerging GaN technologies for power, RF, digital, and quantum computing applications: recent advances and prospects. *J. Appl. Phys.* **130**, 160902 (2021).
4. Fay, P., Jena, D. & Maki, P. (eds) *High-Frequency GaN Electronic Devices* (Springer, 2020).
5. Nomoto, K. et al. GaN/AlN p-channel HFETs with Imax > 420 mA/mm and 20 GHz fT/fMAX. In *Proc. 2020 IEEE International Electron Devices Meeting (IEDM)* 8.3.1–8.3.4 (IEEE, 2020).
6. Bader, S. J. et al. Wurtzite phonons and the mobility of a GaN/AlN 2D hole gas. *Appl. Phys. Lett.* **114**, 253501 (2019).
7. Poncé, S., Jena, D. & Giustino, F. Route to high hole mobility in GaN via reversal of crystal-field splitting. *Phys. Rev. Lett.* **123**, 096602 (2019).
8. Narita, T. et al. Progress on and challenges of p-type formation for GaN power devices. *J. Appl. Phys.* **128**, 090901 (2020).
9. Zheng, Z. et al. Gallium nitride-based complementary logic integrated circuits. *Nat. Electron.* **4**, 595–603 (2021).
10. Bader, S. J. et al. Prospects for wide bandgap and ultrawide bandgap CMOS devices. *IEEE Trans. Electron Devices* **67**, 4010–4020 (2020).
11. Chowdhury, N. et al. p-Channel GaN transistor based on p-GaN/AlGaN/GaN on Si. *IEEE Electron Device Lett.* **40**, 1036–1039 (2019).
12. Khan, M. A., Kuznia, J. N., Van Hove, J. M., Pan, N. & Carter, J. Observation of a two-dimensional electron gas in low pressure metalorganic chemical vapor deposited GaN-$Al_xGa_{1-x}N$ heterojunctions. *Appl. Phys. Lett.* **60**, 3027–3029 (1992).
13. Chaudhuri, R. et al. A polarization-induced 2D hole gas in undoped gallium nitride quantum wells. *Science* **365**, 1454–1457 (2019).
14. Shoenberg, D. *Magnetic Oscillations in Metals* (Cambridge Univ. Press, 2009).
15. Tsukazaki, A. et al. Quantum Hall effect in polar oxide heterostructures. *Science* **315**, 1388–1391 (2007).
16. Ramshaw, B. J. et al. Quasiparticle mass enhancement approaching optimal doping in a high- T_c superconductor. *Science* **348**, 317–320 (2015).
17. Xiang, Z. et al. Quantum oscillations of electrical resistivity in an insulator. *Science* **362**, 65–69 (2018).
18. Lodari, M. et al. Valley splitting in silicon from the interference pattern of quantum oscillations. *Phys. Rev. Lett.* **128**, 176603 (2022).
19. Nichele, F. et al. Spin-orbit splitting and effective masses in p-type GaAs two-dimensional hole gases. *Phys. Rev. B* **89**, 081306 (2014).
20. Hendrickx, N. W. et al. Gate-controlled quantum dots and superconductivity in planar germanium. *Nat. Commun.* **9**, 2835 (2018).
21. Tang, N. et al. Influence of the magnetic field on the effective mass of the two-dimensional electron gas in $Al_xGa_{1-x}N$ /GaN heterostructures. *Phys. Status Solidi C* **3**, 2246–2249 (2006).
22. Tang, N. et al. Abnormal Shubnikov–de Haas oscillations of the two-dimensional electron gas in $Al_xGa_{1-x}N$ /GaN heterostructures in tilted magnetic fields. *Phys. Rev. B* **79**, 073304 (2009).
23. Hang, D. R. et al. Effective mass of two-dimensional electron gas in an $Al_{0.2}Ga_{0.8}N$ /GaN heterojunction. *Appl. Phys. Lett.* **79**, 66–68 (2001).
24. Eisenstein, J. P., Störmer, H. L., Narayanamurti, V., Gossard, A. C. & Wiegmann, W. Effect of inversion symmetry on the band structure of semiconductor heterostructures. *Phys. Rev. Lett.* **53**, 2579–2582 (1984).
25. Habib, B. et al. Spin splitting in GaAs (100) two-dimensional holes. *Phys. Rev. B* **69**, 113311 (2004).

26. Lo, I. et al. Second subband population of the two-dimensional electron gas in strongly coupled GaAs/ $Al_{0.3}Ga_{0.7}$ As double quantum wells. *Phys. Rev. B* **67**, 195317 (2003).
27. Lai, K. Two-flux composite fermion series of the fractional quantum Hall states in strained Si. *Phys. Rev. Lett.* **93**, 156805 (2004).
28. Mironov, O. A. Fractional quantum Hall states in a Ge quantum well. *Phys. Rev. Lett.* **116**, 176802 (2016).
29. Stormer, H. L. Nobel lecture: the fractional quantum Hall effect. *Rev. Mod. Phys.* **71**, 875–889 (1999).
30. Manfra, M. J. et al. High mobility AlGaN/GaN heterostructures grown by plasma-assisted molecular beam epitaxy on semi-insulating GaN templates prepared by hydride vapor phase epitaxy. *J. Appl. Phys.* **92**, 338–345 (2002).
31. Takahide, Y. et al. Quantum oscillations of the two-dimensional hole gas at atomically flat diamond surfaces. *Phys. Rev. B* **89**, 235304 (2014).
32. Sasama, Y. et al. Quantum oscillations in diamond field-effect transistors with a h-BN gate dielectric. *Phys. Rev. Mater.* **3**, 121601 (2019).
33. Horita, M. et al. Hall-effect measurements of metalorganic vapor-phase epitaxy-grown p-type homoepitaxial GaN layers with various Mg concentrations. *Jpn. J. Appl. Phys.* **56**, 031001 (2017).
34. Song, J. O., Ha, J.-S. & Seong, T.-Y. Ohmic-contact technology for GaN-based light-emitting diodes: role of p-type contact. *IEEE Trans. Electron Devices* **57**, 42–59 (2010).
35. Zhang, Z. et al. Polarization-induced 2D hole gases in pseudomorphic undoped GaN/AlN heterostructures on single-crystal AlN substrates. *Appl. Phys. Lett.* **119**, 162104 (2021).
36. Chaudhuri, R., Chen, Z., Muller, D. A., Xing, H. G. & Jena, D. High-conductivity polarization-induced 2D hole gases in undoped GaN/AlN heterojunctions enabled by impurity blocking layers. *J. Appl. Phys.* **130**, 025703 (2021).
37. Bondokov, R. T. et al. Two-inch aluminum nitride (AIN) single crystal growth for commercial applications. *ECS Trans.* **104**, 37 (2021).
38. Cho, Y. et al. Molecular beam homoepitaxy on bulk AlN enabled by aluminum-assisted surface cleaning. *Appl. Phys. Lett.* **116**, 172106 (2020).
39. Lee, K. et al. Surface control and MBE growth diagram for homoepitaxy on single-crystal AlN substrates. *Appl. Phys. Lett.* **116**, 262102 (2020).
40. Dill, J. E., Chang, C. F. C., Jena, D. & Xing, H. G. Two-carrier model-fitting of Hall effect in semiconductors with dual-band occupation: a case study in GaN two-dimensional hole gas. *J. Appl. Phys.* **137**, 025702 (2025).
41. Santic, B. On the hole effective mass and the free hole statistics in wurtzite GaN. *Semicond. Sci. Technol.* **18**, 219–224 (2003).
42. Im, J. S. et al. Radiative carrier lifetime, momentum matrix element, and hole effective mass in GaN. *Appl. Phys. Lett.* **70**, 631–633 (1997).
43. Rodina, A. V. et al. Free excitons in wurtzite GaN. *Phys. Rev. B* **64**, 115204 (2001).
44. Shields, P. A. et al. Free-carrier effects in gallium nitride epilayers: Valence-band dispersion. *Phys. Rev. B* **64**, 081203 (2001).
45. Kasic, A., Schubert, M., Einfeldt, S., Hommel, D. & Tiwald, T. E. Free-carrier and phonon properties of *n*- and *p*-type hexagonal GaN films measured by infrared ellipsometry. *Phys. Rev. B* **62**, 7365–7377 (2000).
46. Feneberg, M. et al. Valence band tomography of wurtzite GaN by spectroscopic ellipsometry. *Appl. Phys. Express* **11**, 101001 (2018).
47. Das Sarma, S. & Stern, F. Single-particle relaxation time versus scattering time in an impure electron gas. *Phys. Rev. B* **32**, 8442–8444 (1985).
48. Chuang, S. L. & Chang, C. S. k.p method for strained wurtzite semiconductors. *Phys. Rev. B* **54**, 2491–2504 (1996).
49. Mireles, F. & Ulloa, S. E. Ordered Hamiltonian and matching conditions for heterojunctions with wurtzite symmetry: GaN/ $Al_xGa_{1-x}N$ quantum wells. *Phys. Rev. B* **60**, 13659–13667 (1999).
50. Jiao, L. et al. Enhancement of the effective mass at high magnetic fields in $CeRhIn_5$. *Phys. Rev. B* **99**, 045127 (2019).
51. Kuszynski, J. E. et al. Effective mass for holes in paramagnetic, plasmonic Cu_5FeS_4 semiconductor nanocrystals. *J. Phys. Chem. C. Nanomater. Interfaces* **126**, 12669 (2022).
52. Falson, J. et al. Electron scattering times in ZnO based polar heterostructures. *Appl. Phys. Lett.* **107**, 082102 (2015).
53. Maryenko, D. et al. Interplay of spin–orbit coupling and Coulomb interaction in ZnO-based electron system. *Nat. Commun.* **12**, 3180 (2021).
54. Tsukazaki, A. et al. Observation of the fractional quantum Hall effect in an oxide. *Nat. Mater.* **9**, 889–893 (2010).
55. Falson, J. & Kawasaki, M. A review of the quantum Hall effects in MgZnO/ZnO heterostructures. *Rep. Prog. Phys.* **81**, 056501 (2018).
56. Sazawa, H. & Yamaguchi, H. High-mobility 2D electron gas in carbon-face 3C-SiC/4H-SiC heterostructure with single-domain 3C-SiC layer. *Appl. Phys. Lett.* **120**, 212102 (2022).
57. Wang, J. et al. THz cyclotron resonance of a 2D hole gas in a GaN/AlN heterostructure. *Appl. Phys. Lett.* **126**, 213102 (2025).
58. Birner, S. et al. nextnano: general purpose 3-D simulations. *IEEE Trans. Electron Devices* **54**, 2137–2142 (2007).
59. Janicki, Ł et al. Electric fields and surface Fermi level in undoped GaN/AlN two-dimensional hole gas heterostructures. *Phys. Status Solidi Rapid Res. Lett.* **15**, 2000573 (2021).
60. Rinke, P. et al. Consistent set of band parameters for the group-III nitrides AlN, GaN, and InN. *Phys. Rev. B* **77**, 075202 (2008).
61. Yan, Q., Rinke, P., Janotti, A., Scheffler, M. & Van de Walle, C. G. Effects of strain on the band structure of group-III nitrides. *Phys. Rev. B* **90**, 125118 (2014).
62. Burt, M. G. Fundamentals of envelope function theory for electronic states and photonic modes in nanostructures. *J. Phys. Condens. Matter* **11**, 53–83 (1999).
63. Bader, S. J. *GaN-on-AlN as a Platform for High-Voltage Complementary Electronics*. PhD thesis, Cornell Univ. (2020); https://doi.org/10.7298/98NJ-7755
64. Vurgaftman, I. & Meyer, J. R. Band parameters for nitrogen-containing semiconductors. *J. Appl. Phys.* **94**, 3675–3696 (2003).
65. Giannozzi, P. et al. Advanced capabilities for materials modelling with Quantum ESPRESSO. *J. Phys. Condens. Matter* **29**, 465901 (2017).
66. Deslippe, J. et al. BerkeleyGW: a massively parallel computer package for the calculation of the quasiparticle and optical properties of materials and nanostructures. *Comput. Phys. Commun.* **183**, 1269–1289 (2012).
67. Mostofi, A. A. et al. wannier90: a tool for obtaining maximally-localised Wannier functions. *Comput. Phys. Commun.* **178**, 685–699 (2008).
68. Ceperley, D. M. Ground state of the electron gas by a stochastic method. *Phys. Rev. Lett.* **45**, 566–569 (1980).
69. Hamann, D. R. Optimized norm-conserving Vanderbilt pseudopotentials. *Phys. Rev. B* **88**, 085117 (2013).
70. Hybertsen, M. S. & Louie, S. G. Electron correlation in semiconductors and insulators: band gaps and quasiparticle energies. *Phys. Rev. B* **34**, 5390–5413 (1986).

Acknowledgements

We thank V. Protasenko for help with the operation of the molecular beam epitaxy system. We thank E. Mueller, N. Harrison,

J. Palmstrom, J. Singleton, L. Winter, C. Yu and R. Chaudhuri for fruitful discussions on quantum transport and epitaxy. We thank D. Deen with Quantinuum for discussions on cryogenic CMOS. C.F.C.C., J.E.D., Z.Z., J.-C.C., S.J.B, J.E., F.G., D.J. and H.G.X are grateful for support by SUPREME, one of seven centres in JUMP 2.0, Semiconductor Research Corporation (SRC) programme sponsored by DARPA. C.F.C.C., J.E.D. and H.G.X. acknowledge support by the NSF FuSe programme, grant no. CMMI-2329063. J.E.D., D.J. and H.G.X. acknowledge support as part of ULTRA, an Energy Frontier Research Center funded by the US Department of Energy (DOE), Office of Science, Basic Energy Sciences (BES), under grant no. DE-SC0021230. N.P., D.A.M., D.J. and H.G.X. acknowledge support by the Army Research Office grant no. W911NF2220177. Characterizations and measurements were performed in part at Cornell NanoScale Facility, a National Nanotechnology Coordinated Infrastructure (NNCI) member supported by NSF grant no. NNCI-2025233. We also made use of the Cornell Center for Materials Research Shared Facilities. The Thermo Fisher Spectra 300 X-CFEG was acquired with support from PARADIM, an NSF MIP (grant no. DMR-2039380) and Cornell University. O.E.A.V., S.A.C., F.F.B., R.D.M. and the National High Magnetic Field Laboratory are supported by the National Science Foundation through grant no. NSF/DMR-2128556, the State of Florida and the US DOE.

Author contributions

H.G.X. and D.J. supervised the project. C.F.C.C. and Z.Z. grew the GaN/AlN epitaxial structures. J.E.D. and J.E. fabricated the Hall bar devices. C.F.C.C., J.E.D., O.E.A.V., F.F.B. and S.A.C. performed the pulsed-field magnetotransport experiments. C.F.C.C. performed the 9 T magnetotransport experiments. N.P. and D.A.M. provided STEM images. C.F.C.C. analysed the magnetotransport data. J.-C.C. and F.G. performed first-principle *GW* calculations. C.F.C.C performed other theoretical calculations. C.F.C.C. wrote the manuscript. C.F.C.C., S.A.C., R.D.M., S.J.B., D.J. and H.G.X. revised the manuscript.

Competing interests

H.G.X., D.J. and S.J.B. are inventors on US patent no. 11158709B2 held by Cornell University, which covers the polarization-induced 2DHG heterostructure used in this study. The remaining authors declare no competing interests.

Additional information

Extended data is available for this paper at https://doi.org/10.1038/s41928-026-01590-8.

Supplementary information The online version contains supplementary material available at https://doi.org/10.1038/s41928-026-01590-8.

Correspondence and requests for materials should be addressed to Chuan F. C. Chang, Debdeep Jena or Huili Grace Xing.

Peer review information *Nature Electronics* thanks Zheyang Zheng and the other, anonymous, reviewer(s) for their contribution to the peer review of this work.

https://doi.org/10.1038/s41928-026-01590-8

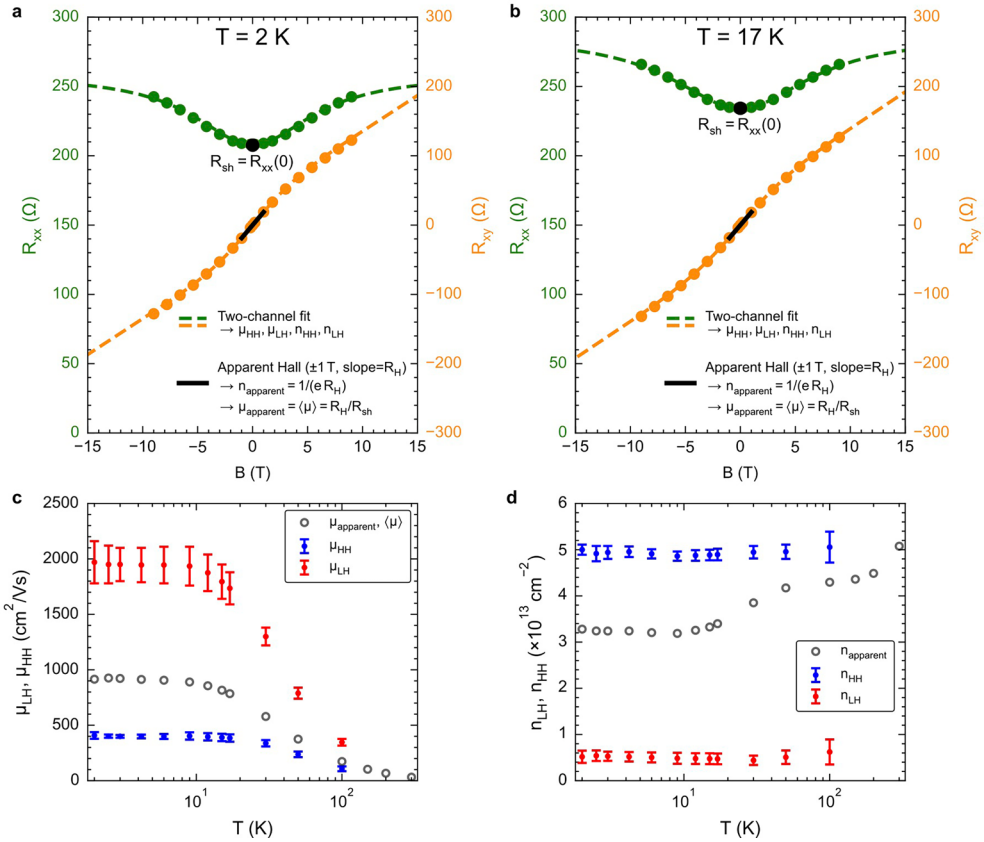

Extended Data Fig. 1 | Low-field magnetotransport measurement and two-channel Drude model fitting. a-b, Longitudinal resistance (R_{xx}) and Hall resistance ($R_{Hall} = R_{xy} = V_{Hall}/I_x$) up to 9 T were measured in a PPMS system using DC current and static magnetic fields. Data for $T = 2$ K (**a**) and $T = 17$ K (**b**) are shown as examples. Solid circles are data, and the dashed lines are fits to a two-channel classical Drude model (see Supplementary Note I). As discussed in Supplementary Note I, table-top Hall effect measurements using a small B (for example, up to ±1 T) give an *apparent* Hall density ($n_{apparent}$) and an *apparent* mobility ($\mu_{apparent}$) based on R_{sh} (R_{xx} at 0 T) and the slope of R_{xy} in the ±1 T range, as shown in (a) and (b); PPMS measurements of R_{xx} and R_{xy} up to 9 T allow for the separation of LH and HH mobilities (**c**) and densities (**d**) via two-channel fitting. Error bars indicate the range spanned by three independent fitting procedures (to $R_{xx}(B)$, to $R_{xy}(B)$, and simultaneously to both); the symbols denote the midpoint of this range. This systematic spread constitutes the primary source of uncertainty as discussed in ref. 40. SdH oscillations were subsequently observed for both LHs and HHs using pulsed magnetic field up to 72 T.

https://doi.org/10.1038/s41928-026-01590-8

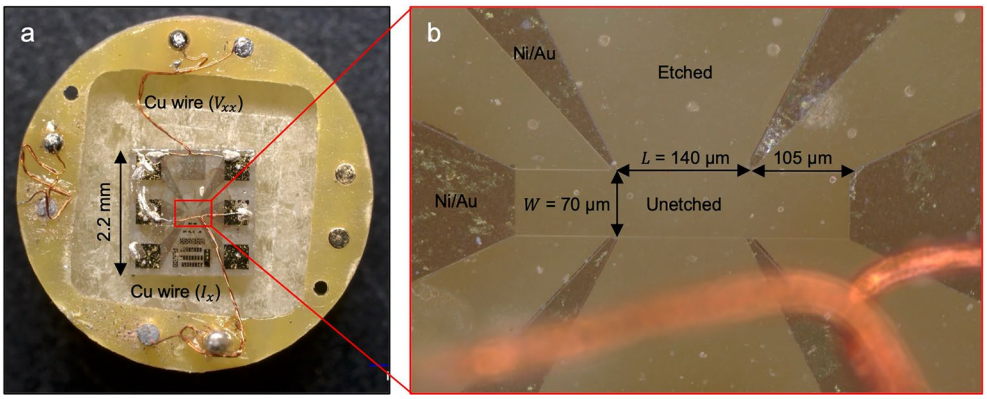

Extended Data Fig. 2 | Fabricated sample with a Hall bar structure. a, Optical micrograph of the fabricated sample mounted on the measurement puck with Cu wires attached as electrical leads for current injection (I_x) and voltage measurement (V_{xx}). **b**, Close-up view of the Hall bar showing its dimensions. The longitudinal resistance R_{xx} is calculated as $R_{xx} = (V_{xx}/I_x) \times (W/L)$.

https://doi.org/10.1038/s41928-026-01590-8

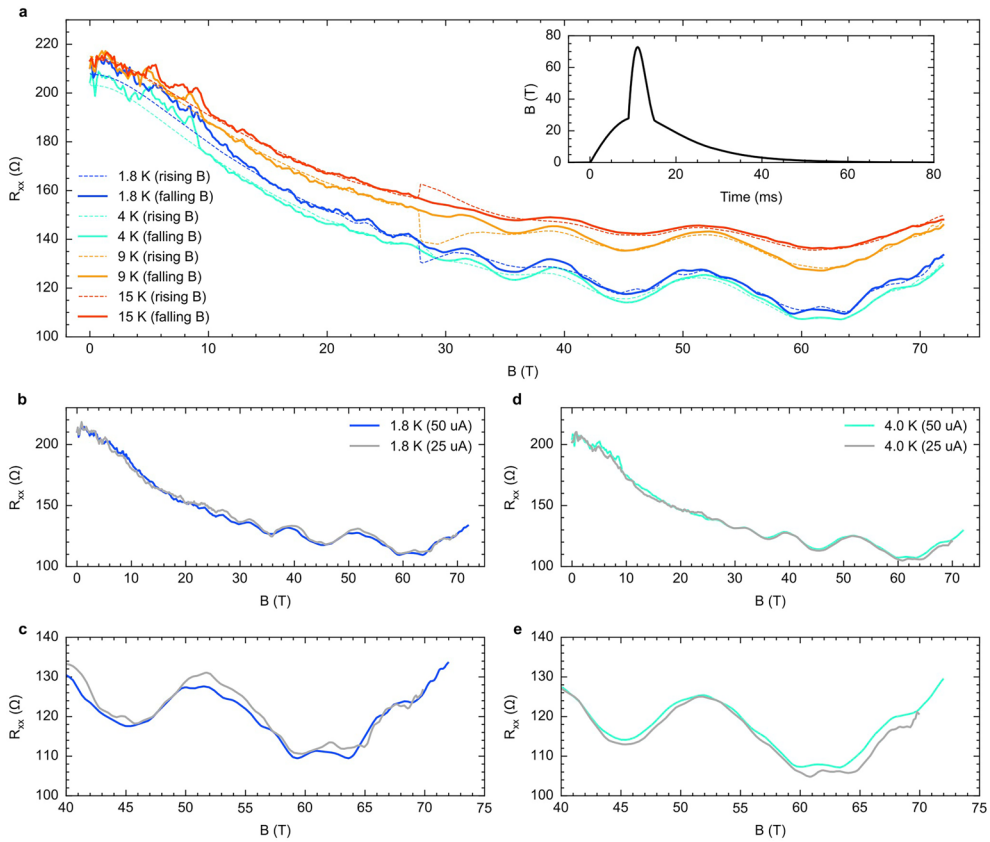

Extended Data Fig. 3 | R_{xx} measured up to 72 T with a 40 kHz AC injection current for lock-in measurement. a, $R_{xx}(B)$ recorded during the rising-field (0 → 72 T, dashed curves) and falling-field (72 → 0 T, solid curves) portions of the pulsed-field measurements (the field sweep profile is shown in the inset). Only four temperatures are shown as examples. **b**-**e**, Falling-field $R_{xx}(B)$ measured at 1.8 K (**b, c**) and 4.0 K (**d, e**) using I^{RMS} = 50 μA (colored) versus I^{RMS} = 25 μA (grey).

https://doi.org/10.1038/s41928-026-01590-8

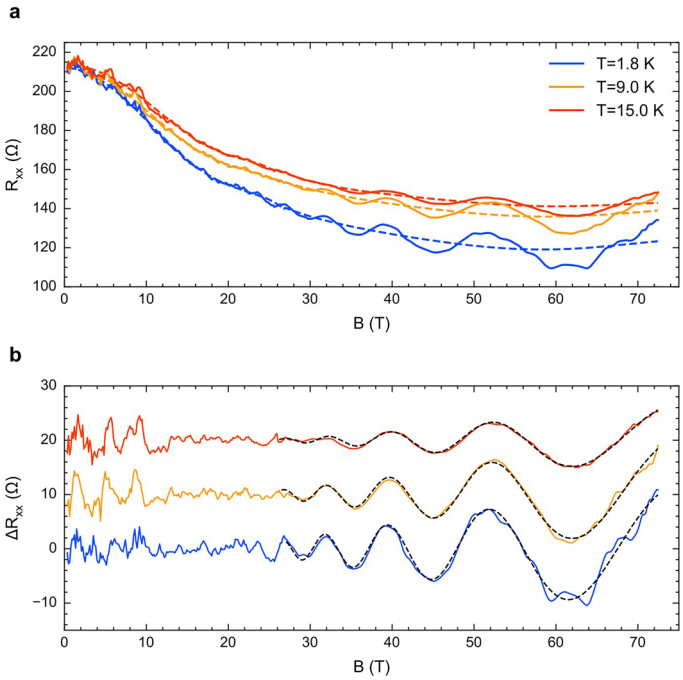

Extended Data Fig. 4 | Background subtraction of R_{xx}. a, Solid lines show the measured R_{xx}, from which a fifth-order polynomial background (dashed lines) is fitted. **b**, Subtracting out the polynomial background yields the combined light hole and heavy hole oscillations (curves offset for clarity). The combined oscillations are then fitted to the single-channel LK equation (black dashed lines) to obtain the LH oscillations which, when subtracted, reveal the HH oscillations shown in Fig. 2c. See Methods and Supplementary Fig. 1 for more details on background subtraction.

https://doi.org/10.1038/s41928-026-01590-8

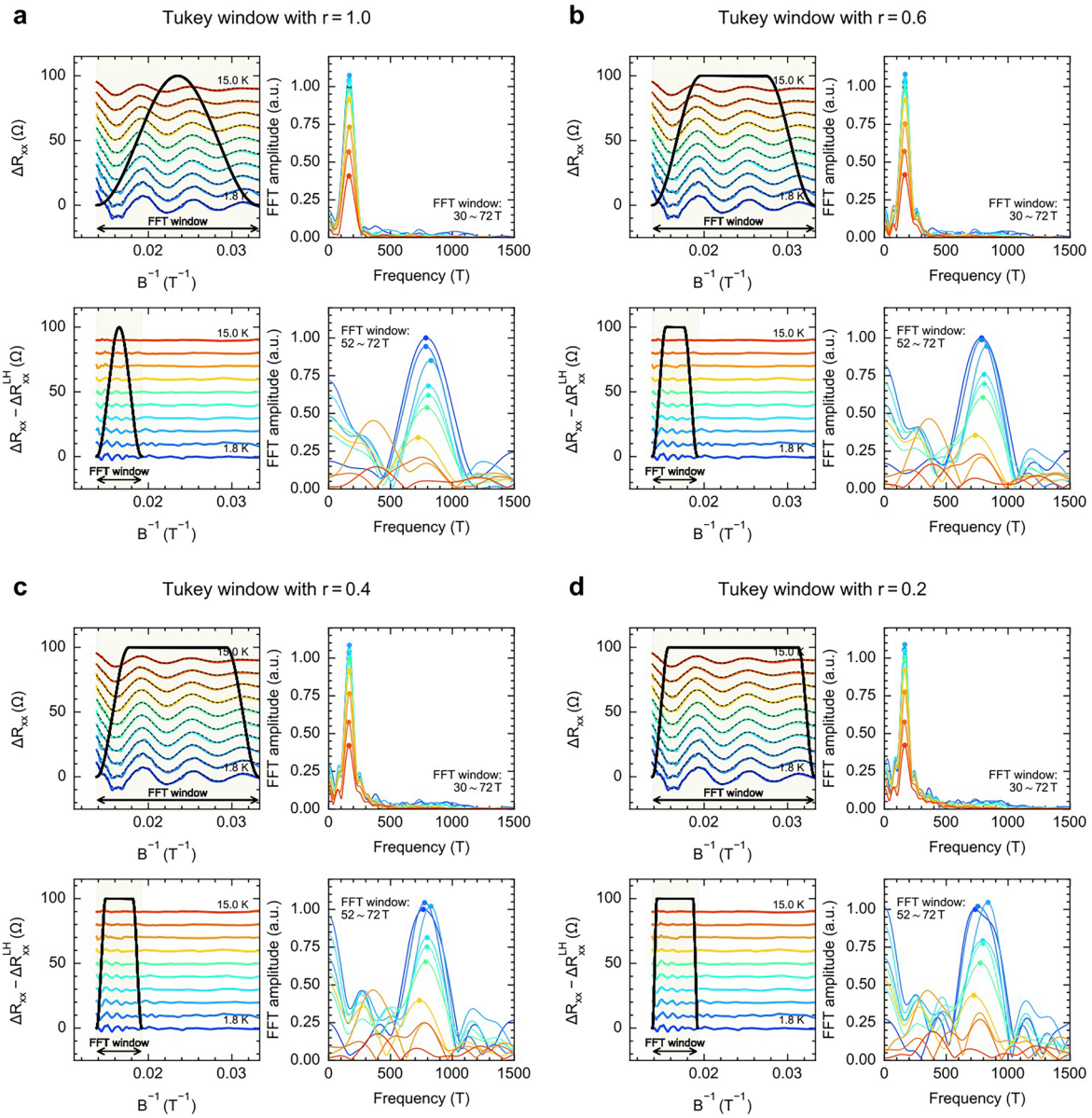

Extended Data Fig. 5 | FFT analysis using different window functions. **a-d**, Prior to performing FFT, both LH and HH oscillation signals (see Fig. 2) are multiplied by Tukey windows (black solid lines) of different r-values—r = 1.0 (**a**), which is the Hanning window; r = 0.8; r = 0.6 (**b**); r = 0.4 (**c**); r = 0.2 (**d**)—to obtain the mean and standard deviation in extracted FFT peak frequencies and amplitudes.

https://doi.org/10.1038/s41928-026-01590-8

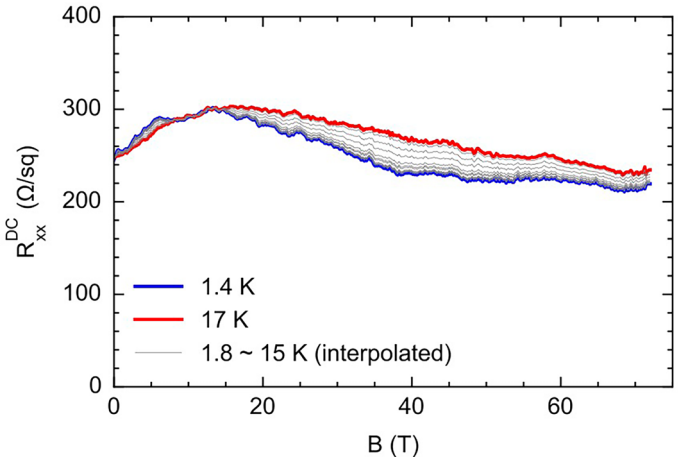

Extended Data Fig. 6 | R_{xx} measured with DC injection current. DC-current measurement of R_{xx} was taken at $T = 1.4$ K (blue) and $T = 17$ K (red) to approximate the true, undistorted background resistance R_{xx}^{bg} (see Methods). A simple linear interpolation was used to approximate $R_{xx}^{bg}(B,\ T)$ at intermediate temperatures between 1.4 K and 17 K (grey).

https://doi.org/10.1038/s41928-026-01590-8

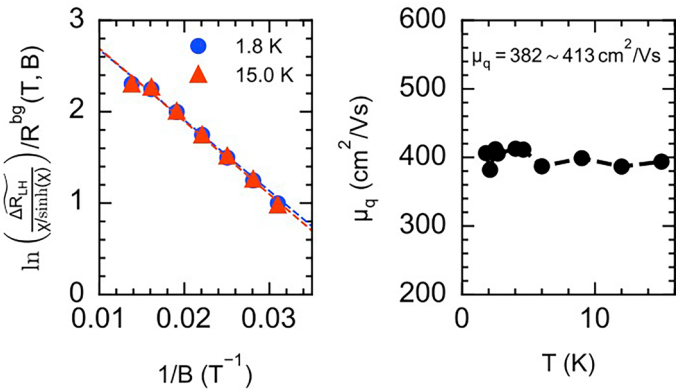

Extended Data Fig. 7 | Extraction of the quantum mobility μ_q. (**Left**) Dingle plot of the LH oscillation peaks at 1.8 K and 15 K. $\widetilde{\Delta R_{LH}} = \frac{\Delta R_{LH}}{R^{bg}(T,B)}$ is the background-normalized light hole oscillation amplitude. A linear fit (dashed line, with slope s) gives the quantum mobility as $\mu_q = -\pi/s$. (**Right**) μ_q as a function of temperature, showing no discernable temperature dependence.

https://doi.org/10.1038/s41928-026-01590-8

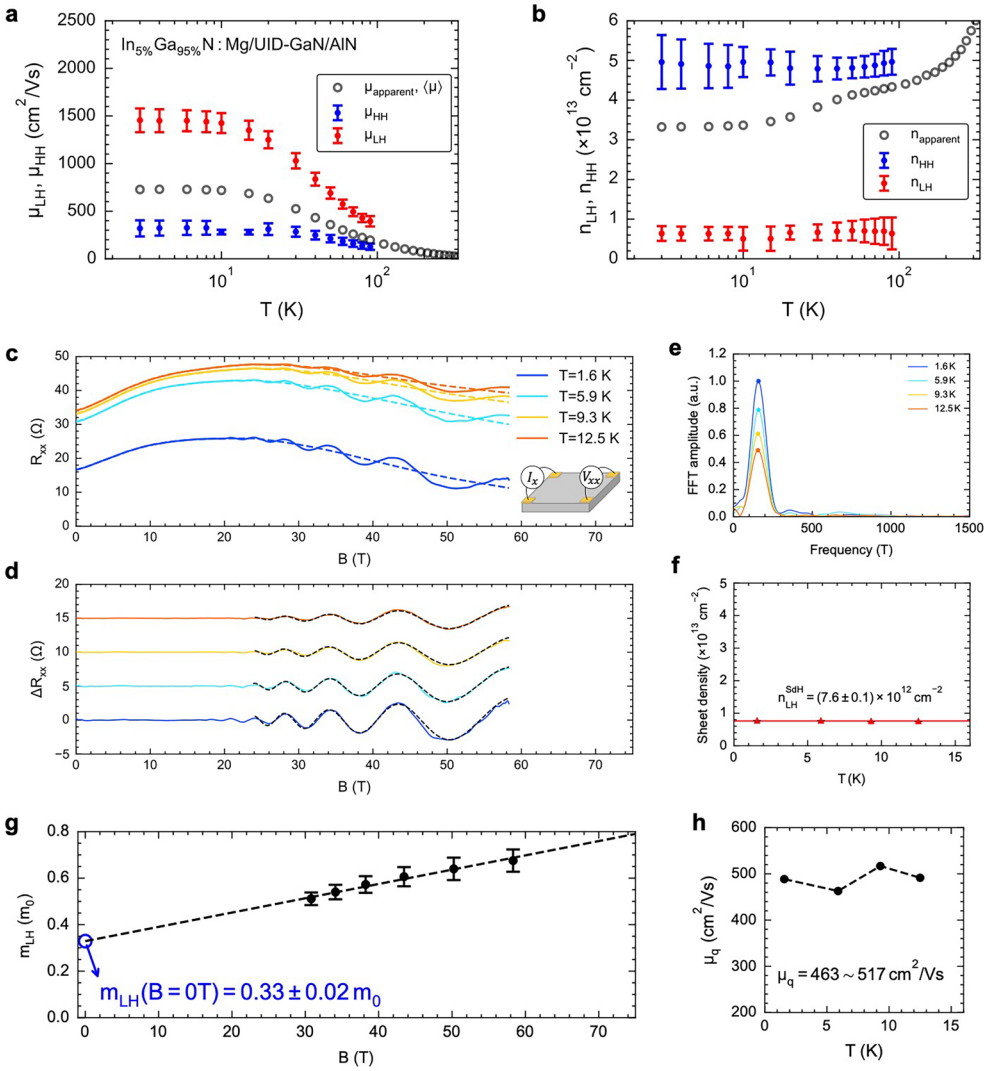

Extended Data Fig. 8 | Summary of electrical transport results for a similar sample consisting of InGaN:Mg/UID-GaN/AlN measured in a van der Pauw geometry. a, b, Analysis of two-channel fitting of Hall measurements up to 9 T. See the caption of Extended Data Fig. 1 for more description, including the definition of the plotted error bars. **c-h**, Data and analysis of 58 T pulsed-field measurements showing LH SdH oscillations. See the captions of Fig. 2 and Fig. 4 for more description, including the definition of the numerical uncertainties and plotted error bars.

https://doi.org/10.1038/s41928-026-01590-8

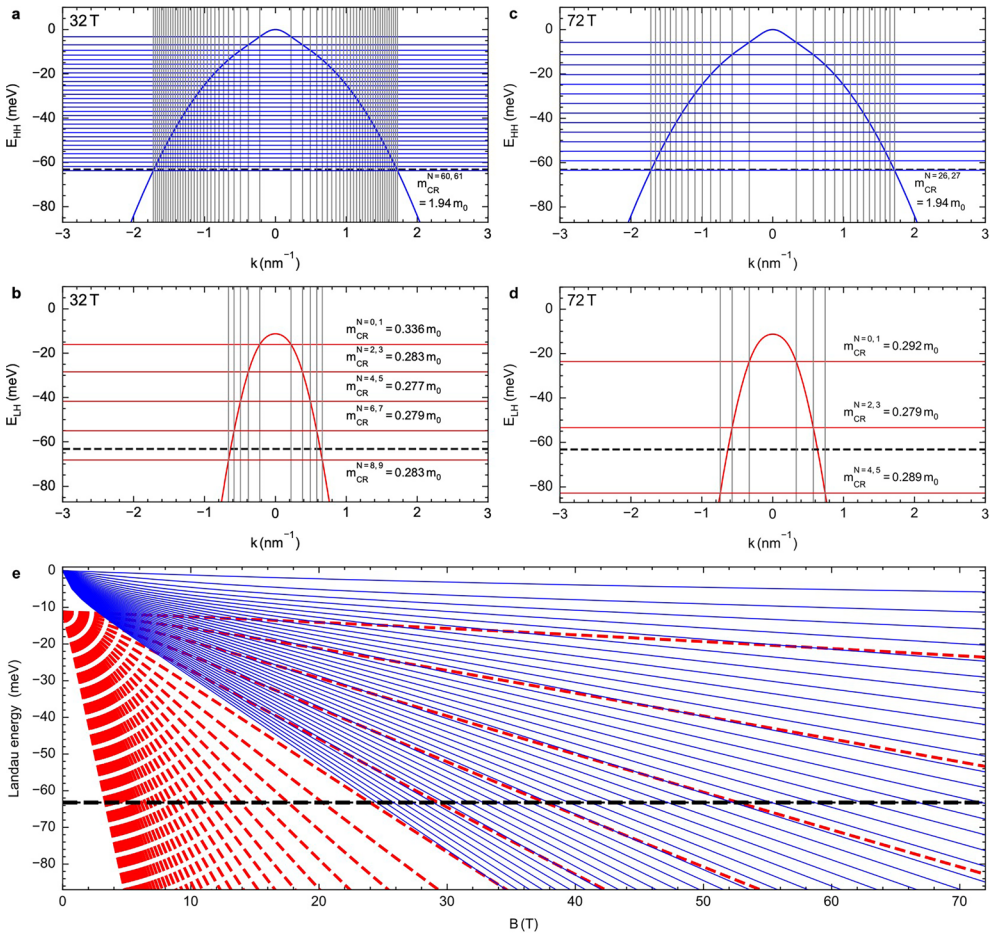

Extended Data Fig. 9 | Landau level calculations. a-d, The quantized wave vectors k (vertical lines) were calculated for $B = 32$ T (**a-b**) and $B = 72$ T (**c-d**) as described in Methods. Their intersections with the HH (**a,c**) and LH (**b,d**) dispersions determine the LLs. Only the occupied LLs and the lowest unoccupied LL are shown. **e**, The Landau fan diagram showing the LLs for HH (solid blue lines) and LH (dashed red lines). Despite band nonparabolicity, both LH and HH LLs are approximately uniformly spaced near E_F. Consistently, the cyclotron masses of the LLs near E_F converge to 0.28–0.29 m_0 for LH and 1.94 m_0 for HH at both magnetic fields.

https://doi.org/10.1038/s41928-026-01590-8

Extended Data Table 1 | Material parameters used for *k·p* band structure and energy band diagram calculations shown in Fig. 1c, Fig. 3 and Extended Data Fig. 9

Parameter	GaN	AlN
Lattice constants[64]		
$a^{300\,K}$ (Å)	3.189	3.112
$c^{300\,K}$ (Å)	5.185	4.982
Band gap[64]		
E_g(eV)	3.510	6.25
Varshni parameters[64]		
α (meV/K)	0.909	1.799
β (K)	830	1462
Crystal-field splitting[64]		
Δ_{CR} (eV)	0.010	-0.169
Spin-orbit splitting[64]		
Δ_{SO} (eV)	0.017	0.019
Rashba-Sheka-Pikus k.p parameters[60]		
A_1	-5.947	-3.991
A_2	-0.528	-0.311
A_3	5.414	3.671
A_4	-2.512	-1.147
A_5	-2.510	-1.329
A_6	-3.202	-1.952
Deformation potentials[61]		
a_{cz} (eV)	-11.3	-11.8
a_{ct} (eV)	-4.9	-3.4
$a_{cz} - D_1$ (eV)	-6.07	-4.36
$a_{ct} - D_2$ (eV)	-8.88	-12.35
D_3 (eV)	5.38	9.17
D_4 (eV)	-2.69	-3.72
D_5 (eV)	-2.56	-2.93
D_6 (eV)	-3.88	-4.58
Elastic moduli[64]		
C_{11} (GPa)	390	396
C_{12} (GPa)	145	137
C_{13} (GPa)	106	108
C_{33} (GPa)	398	373
C_{44} (GPa)	105	116
Spontaneous polarization constant[63]		
P_{sp} (C/m^2)	1.327	1.341
Piezoelectric polarization constants[63]		
e_{33} (C/m^2)	1.02	1.569
e_{31} (C/m^2)	-1.863	-2.027
e_{51} (C/m^2)	0.3255	0.4176